metals

MDPI

Review

Interstitial Atom Engineering in Magnetic Materials

Jiro Kitagawa [1,*], Kohei Sakaguchi [1], Tomohiro Hara [1], Fumiaki Hirano [1], Naoki Shirakawa [2] and Masami Tsubota [3]

[1] Department of Electrical Engineering, Faculty of Engineering, Fukuoka Institute of Technology, 3-30-1 Wajiro-higashi, Higashi-ku, Fukuoka 811-0295, Japan; s1451020@bene.fit.ac.jp (K.S.); s1552037@bene.fit.ac.jp (T.H.); s1652044@bene.fit.ac.jp (F.H.)

[2] Flexible Electronics Research Center, National Institute of Advanced Industrial Science and Technology, Tsukuba, Ibaraki 305-8565, Japan; shirakawa.n@aist.go.jp

[3] Physonit Inc., 6-10 Minami-Horikawa, Kaita Aki, Hiroshima 736-0044, Japan; tsubota@physonit.jp

* Correspondence: j-kitagawa@fit.ac.jp; Tel.: +81-(0)92-606-4579

Received: 17 November 2020; Accepted: 3 December 2020; Published: 6 December 2020

Abstract: Interstitial light elements play an important role in magnetic materials by improving the magnetic properties through changes of the unit cell volume or through orbital hybridization between the magnetic and interstitial atoms. In this review focusing on the effects of interstitial atoms in Mn-based compounds, which are not well researched, the studies of interstitial atoms in three kinds of magnetic materials (rare-earth Fe-, Mn-, and rare-earth-based compounds) are surveyed. The prominent features of Mn-based compounds are interstitial-atom-induced changes or additional formation of magnetism—either a change from antiferromagnetism (paramagnetism) to ferromagnetism or an additional formation of ferromagnetism. It is noted that in some cases, ferromagnetic coupling can be abruptly caused by a small number of interstitial atoms, which has been overlooked in previous research on rare-earth Fe-based compounds. We also present candidates of Mn compounds, which enable changes of the magnetic state. The Mn-based compounds are particularly important for the easy fabrication of highly functional magnetic devices, as they allow on-demand control of magnetism without causing a large lattice mismatch, among other advantages.

Keywords: interstitial atom; Mn-based compounds; rare-earth Fe-based compounds; rare-earth-based compound; Bethe–Slater curve; ferromagnetic; antiferromagnetic; permanent magnet

1. Introduction

Some crystal structures possess interstitial crystallographic sites, which light elements such as hydrogen, boron, carbon, nitrogen, and oxygen atoms can occupy. There is a rather long history of metallurgical, physical, and chemical research studies on interstitial atoms [1,2]. In past years, domain control of ferromagnets has been studied [1]. Since the 1980s, interstitial atoms have attracted intense attention related to the improvement of magnetic properties of rare-earth Fe and Co-based permanent magnets [2–6].

Interstitial atoms have two major roles—influencing the stability of the crystal structure and in the modification or change in magnetic properties. In the former case, small amounts of interstitial light elements are required to stabilize the desired crystal structure; compounds without interstitial atoms would not exist in thermal equilibrium. In the latter case, interstitial atoms affect the crystal structure parameters, such as the interatomic distances between magnetic atoms or the orbital hybridization between magnetic and interstitial atoms, consequently meaning the magnetic ordering temperature, the magnetic moment, the magnetic structure, and other factors can be altered.

The most well-studied platforms for interstitial atoms are rare-earth Fe-based permanent magnets. The improvements of the magnetic properties have mainly been achieved through the addition of light

elements such as boron, carbon, and nitrogen atoms. The Bethe–Slater curve is one of the criteria needed to understand whether metal 3*d* transition elements of Cr, Mn, Fe, Co, and Ni possess ferromagnetic (FM) or antiferromagnetic (AFM) states (see Figure 1) [7–10]. This curve exhibits the exchange coupling as a function of the interatomic distance. Fe falls in the FM region near to the border between FM and AFM states. Therefore, in Fe-based compounds, a shorter Fe–Fe distance (shrinkage of the unit cell volume) favors an AFM state, while a longer Fe–Fe distance (an expansion of the unit cell volume) favors the FM state [11–13]. With increasing Fe–Fe distance, smaller overlapping of 3*d* wave functions makes the 3*d* band narrower, which leads to the FM state, and in most cases the Curie temperature T_C is enhanced.

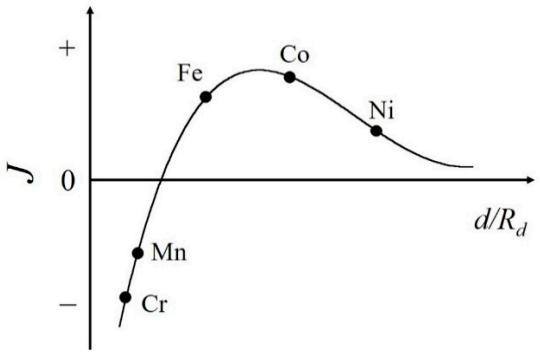

Figure 1. Schematic view of the Bethe–Slater curve. Here, *J*, *d*, and R_d represent the magnetic exchange coupling between atoms, the interatomic distance, and the radius of the 3*d* shell, respectively.

On the other hand, the effects of interstitial atoms in Mn-based compounds are not well researched. As shown in Figure 1, the Mn atom itself shows the AFM ground state, however the expanded Mn–Mn distance in Mn-based compounds leads to the FM state. Mn compounds are indispensable for both FM and AFM materials. For example, MnBi and MnAl have attracted much attention as permanent magnets [14–18]. MnSi has been extensively studied as a magnetic material with a skyrmion state, which is a noncollinear magnetic structure. The skyrmion domains can be driven by the low current density threshold [19]. Recently, Mn_3Sn has been intensively studied as a topological antiferromagnet [20] and is a candidate next-generation spintronics material. If the effects of interstitial atoms are well understood, they can be highly useful in the development of spintronics devices or highly functional magnetic devices, which can be developed via easy on-demand control of the magnetic state.

In this review, we present information on the effects of interstitial atoms in rare-earth Fe-, Mn-, and rare-earth-based compounds, especially focusing on Mn-based compounds. We introduce the frequently studied Mn-based compounds, showing the changes of magnetic states caused by the interstitial atoms, as well as our recent results. Interestingly, a change in the magnetic ground state or an additional formation of the FM state caused by interstitial atoms is possible. Specifically, our results highlight an abrupt emergence of FM exchange coupling above room temperature caused by the addition of a small amount of light elements, which has not been clearly reported for rare-earth Fe-based compounds. Additionally, candidate crystal structures for Mn compounds are presented, in which a magnetic state can be changed using interstitial atoms. Finally, perspectives concerning the development of magnetic devices based on Mn-based compounds and the strategy for further improvement of magnetic properties are outlined.

2. Rare-Earth Fe-Based Compounds

2.1. Th_2Zn_{17}-Type

$R_2Fe_{17}N_x$ (R = light rare-earth) represents the permanent magnets with the hexagonal Th_2Zn_{17}-type structure (space group: $R\bar{3}m$, No. 166). There is an interstitial Wyckoff position 9*e* for nitrogen

atoms. The roles of nitrogen atoms are the enhancement of T_C and the saturated magnetization M_s and the change in magnetic anisotropy. For example, T_C = 389 K and M_s = 1.00 T at a room temperature of Sm_2Fe_{17} are increased to 749 K and 1.54 T, respectively, in $Sm_2Fe_{17}N_3$ (see Table 1). Moreover, the in-plane anisotropy in Sm_2Fe_{17} is changed to uniaxial anisotropy by the nitriding, which is advantageous for application as permanent magnets.

Table 1. The magnetic and structural properties of rare-earth Fe-based compounds with and without interstitial atoms, where *a* and *c* are the lattice parameters, and *V* is the unit cell volume. RT means the room temperature. Data are from the references listed in the table.

Compound	T_C (K)	M_S @RT (T)	Easy Magnetization Direction	*a* (Å)	*c* (Å)	*V* (Å^3)	Ref.
Sm_2Fe_{17}	389	1.00	in-plane	8.55	12.45	788.2	[21,22]
$Sm_2Fe_{17}N_3$	749	1.54	c axis	8.74	12.70	840.2	[23,24]
$Sm_2Fe_{17}C_3$	668	1.43	c axis	8.744	12.572	832.4	[25,26]
$SmFe_{11}Ti$	584	1.15	c axis	8.56	4.80	351.7	[27,28]
$SmFe_{11}TiN$	769	1.28	in-plane	8.64	4.84	361.3	[28,29]
$NdFe_{11}Ti$	547	1.38	in-plane	8.585	4.789	353.0	[30,31]
$NdFe_{11}TiN$	729	1.48	c axis	8.701	4.844	366.7	[32,33]
$SmFe_9Si_2C_{1.0}$	462	0.88	c axis	10.057	6.512	658.7	[34]
$SmFe_9Si_2C_{1.5}$	492	0.90	c axis	10.082	6.554	666.1	[34]

The addition of nitrogen atoms expands the lattice parameters *a* and *c*, resulting in the increased Fe–Fe interatomic distance and the enhancement of T_C. Actually, in $Sm_2Fe_{17}N_3$, T_C is almost doubled, which is much larger than that in the case of $ThMn_{12}$-type compounds (see also Section 2.2 and Table 1). The difference is well correlated with the rate of unit-cell-volume change $\Delta V/V$ by the interstitial atoms, which is defined by

$$\frac{\Delta V}{V} = \frac{V_w - V_{w/o}}{V_{w/o}} \times 100 \quad (1)$$

where $V_{w/o}$ and V_w are the unit cell volumes without and with interstitial atoms, respectively. We note here that the compound without interstitial atoms is hereafter often called the parent compound. For example, $\Delta V/V$ = 6.6% in $Sm_2Fe_{17}N_3$ is larger than that in $ThMn_{12}$-type $SmFe_{11}TiN$ (2.7%). The larger $\Delta V/V$ for $Sm_2Fe_{17}N_3$ is ascribed to the fact that Fe magnetic moments in the Th_2Zn_{17}-type structure are less itinerant.

2.2. *$ThMn_{12}$-Type*

The well studied system is $RFe_{11}Ti$ (R: rare-earth) series (*I*4/*mmm*, No. 139). This structure allows the interstitial nitrogen atoms to occupy the 2*b* site. In $SmFe_{11}TiN$ or $NdFe_{11}TiN$, the nitrogen addition enhances T_C by about 30%, which is smaller than that of the Th_2Zn_{17}-type system (see Table 1). As mentioned above this is due to the smaller $\Delta V/V$ under the addition of nitrogen (2.7% for $SmFe_{11}TiN$ and 3.9% for $NdFe_{11}TiN$). The magnetic anisotropy of $RFe_{11}Ti$ is determined primarily due to the single-ion contribution of R ion, thus $NdFe_{11}Ti$ and $SmFe_{11}Ti$ show the planar and *c* axis anisotropies, respectively. In each compound, the sign of magnetic anisotropy constant K_1 is reversed by the nitrogen addition and a good candidate of the permanent magnet is consequently $NdFe_{11}TiN$.

The first-principle studies have revealed that $NdFe_{12}N$, which possesses an Fe concentration higher than that of $NdFe_{11}TiN$ and is more favorable for a permanent magnet, has excellent magnetic properties [35–37], however, it is thermodynamically unstable in bulk form. The thin film fabrication allows the growth of $NdFe_{12}N_x$, which shows a superior M_s = 1.7 T compared to Nd–Fe–B magnets [38]. The coercivity of $NdFe_{12}N_x$ is rather low, however, a born doped $Sm(Fe_{0.8}Co_{0.2})_{12}$ is recently reported to be a highly coercive material with 1.2 T [39]. The microstructure of the compound exhibits columnar-shaped $Sm(Fe_{0.8}Co_{0.2})_{12}$ grains, surrounded by a born-rich amorphous phase. The domain wall pinning at the grain boundary is responsible for the high coercivity [39].

Mao et al. reported a *BH* energy product of $ThMn_{12}$-type compound [40]. They have investigated the magnetic properties of powdered $PrFe_{12-x}V_x$ and the nitride compound. $Pr(Fe, V)_{12}N_{1.6}$ exhibits the maximum *BH* energy product of 135 kJ/m^3.

2.3. $BaCd_{11}$-Type

The tetragonal $BaCd_{11}$-type structure represented by $RFe_9Si_2C_x$ (Table 1) is a candidate for a next-generation rare-earth Fe-based permanent magnet. It is interesting that the addition of carbon atoms is required to stabilize the $BaCd_{11}$-type structure. In $RFe_9Si_2C_x$, the carbon atom occupies the interstitial 8*c* site of the tetragonal space group of $I4_1/amd$ (No. 141). T_C progressively increases with the increase of x, for example, T_C = 367 K of $SmFe_9Si_2C_{0.5}$ is enhanced to 492 K in $SmFe_9Si_2C_{1.5}$, accompanying the volume expansion [30]. The magnetic anisotropy depends on the R atom; in-plane anisotropy is observed in R = Ce or Nd, whilst on the other hand, R = Sm possesses the *c* axis anisotropy.

2.4. Remark on Hybridization Effect

Through the extensive studies of rare-earth Fe-based permanent magnets, it is revealed that stronger orbital hybridization in the covalent bond between Fe and an interstitial atom tends to reduce the magnetic moment. The strength of the covalent bond is well reflected by $\Delta V/V$ under the addition of light elements; $\Delta V/V$ is not so large when the hybridization is stronger. $\Delta V/V$ is generally larger for the nitrogen addition compared to the carbon one (see, for example, $Sm_2Fe_{17}N_3$ and $Sm_2Fe_{17}C_3$ in Table 1).

3. Mn-Based Compounds

In this section, we gathered as many Mn-based room temperature ferromagnets as possible.

3.1. Hydrogen-Absorbed (R or Th)$_6Mn_{23}$

R_6Mn_{23} (R = rare earth) series and Th_6Mn_{23} crystallize into the cubic Th_6Mn_{23}-type structure with the space group $Fm\bar{3}m$ (No. 225). R atoms occupy the 24*e* site, and Mn atoms the 4*b*, the 24*d* and the two 32*f* sites. All R_6Mn_{23} compounds show FM orderings at a T_C higher than 300 K, which are induced by Mn magnetic moments. On the other hand, Th_6Mn_{23} remains a paramagnet down to low temperatures. The hydrogen absorption generally expands the unit cell volume (see Figure 2 and Table 4), whereas the occupation site of the hydrogen atom is not clear. Although the T_C of non-hydrogenated R_6Mn_{23} rises with increasing volume, most of the hydrogen-absorbed compound shows the suppressed T_C compared to each parent compound. For example [41], T_C = 461 K of Gd_6Mn_{23} is reduced to T_C = 2.66 K in $Gd_6Mn_{23}H_x$. The saturated moment is also highly reduced (49 μ_B/f.u. to 14.2 μ_B/f.u.) [41]. The opposite behavior is confirmed for Th_6Mn_{23}, in spite of the similar volume change by the hydrogenation. The hydrogenated Th_6Mn_{23} shows an emergence of ferromagnetism with T_C = 335 K, although the saturated moment of Mn is not so high (16.5 μ_B/f.u.) [41]. Considering that R and Th ions are in the trivalent and the tetravalent state, respectively, the exchange coupling between Mn magnetic moments would significantly depend on the valence electron count per atom (VEC). We note that Th_6Mn_{23} is the typical Mn-based compound showing the change in magnetic state by interstitial atoms. The saturated moment induced in the FM state of the hydrogenated compound is rather low, indicating a strong orbital hybridization between Mn and hydrogen atoms and/or a complex magnetic structure.

3.2. Hydrogen-Absorbed YMn_2

The crystal structure of YMn_2 is the cubic $MgCu_2$-type structure with the space group of $Fd\bar{3}m$ (No. 227). Y and Mn atoms occupy the 8*a* and the 16*d* site, respectively. YMn_2 can absorb hydrogen atoms as in R_6Mn_{23}. Although YMn_2 is paramagnetic down to low temperatures, YMn_2H_x shows a lattice expansion under hydrogenation, which induces a ferromagnetism with T_C = 284 K and a

saturation moment of 0.52 μ_B/f.u. [41]. There are many RMn_2 compounds with the same structure, however, we do not make the magnetic ordering temperature vs. unit cell volume plot, because the accurate nature of the magnetic order is still unknown for each compound [42]. YMn_2 can also be regarded as the compound, realizing the change from paramagnetism to ferromagnetism by interstitial atoms.

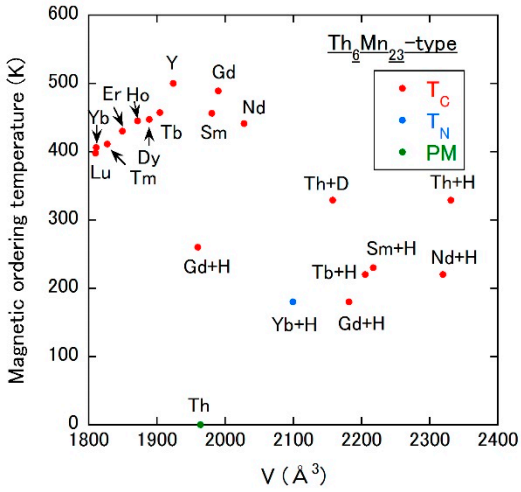

Figure 2. Magnetic ordering temperature vs. unit cell volume plot of Th_6Mn_{23}-type Mn compounds. T_N is the Néel temperature. PM means the paramagnetic state. For example, Th + H (Th + D) means the hydrogen (deuterium)-absorbed Th_6Mn_{23}.

3.3. Carbon-Added Mn_5Si_3

This system shows a change from the AFM to FM state by the carbon addition. The hexagonal Mn_5Si_3-type structure is known as a superior platform for studying interstitial chemistry [43]. The space group is $P6_3/mcm$ (No. 193), in which the Wyckoff positions are the 4*d* for Mn1, the 6*g* for Mn2 and the 6*g* for Si (see also Figure 3a). Carbon atoms occupy the 2*b* site. While the parent compound Mn_5Si_3 shows an AFM ordering at the Néel temperature T_N = 98 K, a thin film $Mn_5Si_3C_x$ becomes a room-temperature ferromagnet with T_C = 350 K as shown in Figure 3b (see the filled squares) [44,45]. In [44], the appearance of the FM state is ascribed to the enhanced Mn–Mn interaction mediated by added carbon. Associated with the unit cell volume expansion by the carbon addition, the saturation Mn moment rapidly increases to 1 μ_B/Mn at x = 0.75 (see Figure 3c). However, the x dependence of T_C is peculiar: a T_C plateau of 350 K in a rather wide x range, where the saturation Mn moment is steadily reduced as x is increased above 0.75. We speculate that the hybridization between Mn2 and C atoms is strong, due to the short Mn2–C distance (see Figure 3a). As x is increased, the magnetic moment of Mn2 would be decreased, but that of Mn1 under well localized state due to the weak influence of the carbon addition would be enhanced. The rather strong Mn1–Mn1 magnetic interaction would be responsible for the plateau of T_C, while the decreasing Mn2 moment with increasing x would contribute to the reduction in the saturation moment.

3.4. (R or Actinide)Mn_2Si_2 and Its Germanides

Despite the absence of a report on the addition of light elements in these compounds, the magnetic ordering temperature vs. unit cell volume plot shows the thought-provoking results as shown in Figure 4. These compounds possess the tetragonal $ThCr_2Si_2$-type structure (*I*4/*mmm*, No. 139), where Mn atoms at the 4*d* sites form the layered structure perpendicular to the *c* axis. R (Actinide) and Si (Ge) atoms occupy the 2*a* and the 4*e* sites, respectively. In the case of RMn_2Si_2, only the R = La compound exhibits an FM state and the other compounds AFM one (see 21–35 in Figure 4). When Si is replaced by Ge, FM (AFM) states are observed for R = La to Sm (R = the other elements) as shown in

36–47 of Figure 4. Figure 4 provides a good correlation between the magnetic ordering temperature and the unit cell volume throughout the two series: systematically descending ordering temperature with expanding volume. Furthermore, magnetic structure changes from AFM to FM at approximately 179 Å^3, which is consistent with the picture of the Bethe–Slater curve. The inverse trend is confirmed in (U or Th)Mn_2Si_2 and its germanide (see 48 and 49 (50 and 51) in Figure 4), that is, the crossover from the FM to AFM state occurs by increasing the volume in each system. This can be ascribed to the difference of valence between rare-earth (trivalent) and actinide (maybe tetravalent) elements as in the case of Th_6Mn_{23}-type compounds.

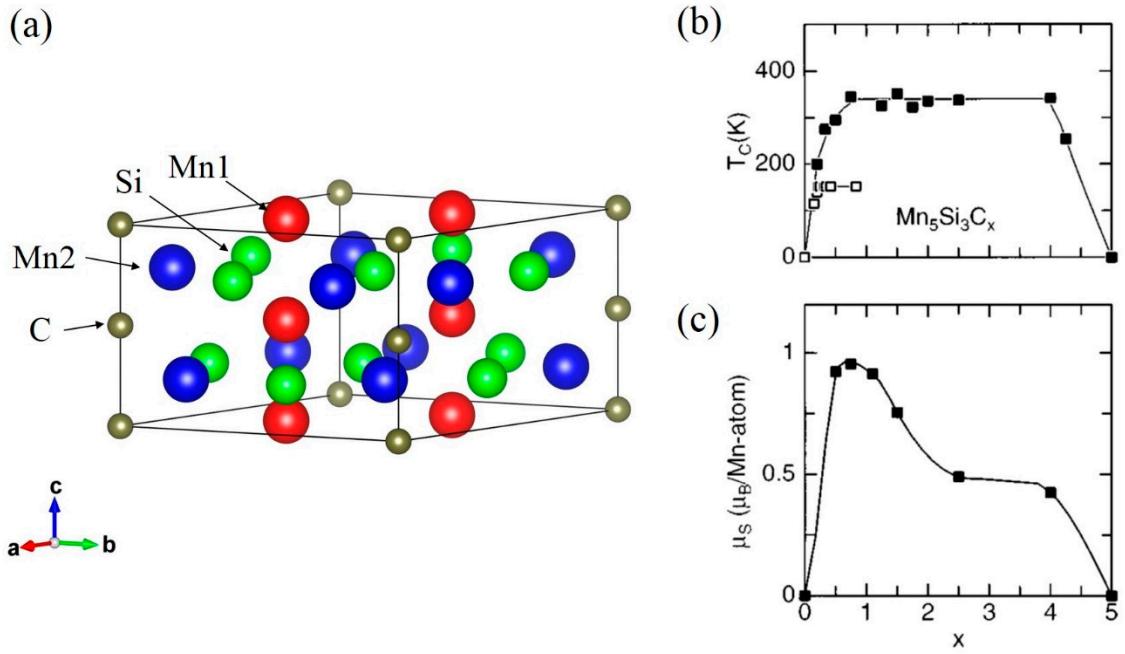

Figure 3. (**a**) Crystal structure of $Mn_5Si_3C_x$, where the solid line represents the unit cell. x dependence of (**b**) T_C and (**c**) the saturation magnetic moment for $Mn_5Si_3C_x$. In (**b**), the filled and the open squares indicate the thin film and bulk samples, respectively. Reproduced with permission from [44].

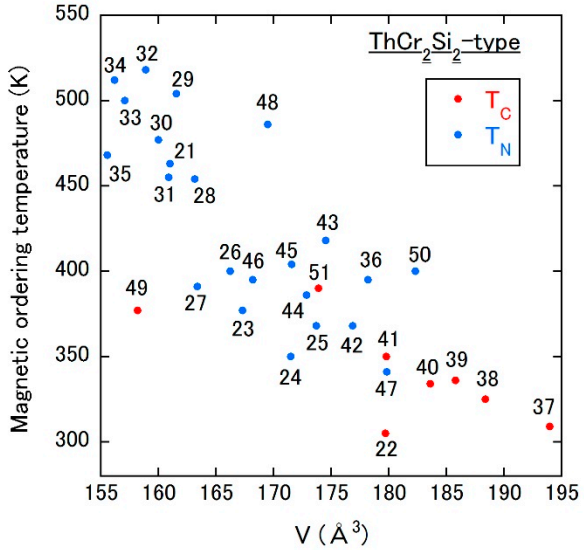

Figure 4. Magnetic ordering temperature vs. unit cell volume plot of $ThCr_2Si_2$-type Mn compounds. The numbers in the figure correspond to those in Table 4 (21–47 for R-containing compounds, and 48–51 for U- or Th-containing compounds).

3.5. Boron-Added $Pd_{0.75}Mn_{0.25}$ Alloy

The disordered face-centered-cubic (fcc) $Pd_{1-x}Mn_x$ alloys are the well studied spin-glass system [46]. The crystal structure is described by the space group of $Fm\bar{3}m$ (No. 225), possessing only the 4*a* site (see Figure 5), that is randomly occupied by Pd and Mn atoms. At $x = 0.25$, the spin-glass transition temperature T_{SG} is 45 K [47]. The $Pd_{0.75}Mn_{0.25}$ alloy can incorporate boron atoms [48,49] with the solubility limit of approximately x ~ 0.16 in $Pd_{0.75}Mn_{0.25}B_x$. According to the structure report [50] of PdH_x with the same structure, interstitial atoms prefer the octahedral sites (the 4*b* site, see Figure 5). The volume expansion occurs with the increase of x as shown in Table 2. Figure 6a shows the isothermal magnetization curves of $Pd_{0.75}Mn_{0.25}B_x$ at room temperature, which demonstrate the emergence of room temperature ferromagnetism by the slight addition of boron atoms. To elucidate the impact of the boron addition on the effective magnetic moment of Mn atoms, temperature dependences of inverse dc magnetization $1/\chi_{dc}$ are measured as shown in Figure 6b. All measured samples follow the Curie–Weiss law above T_C (see the solid lines in Figure 6b, and the extracted effective magnetic moment μ_{eff} and the Weiss temperature θ are summarized in Table 2). μ_{eff} of the parent compound is 4.85 μ_B/Mn, which is once reduced by the boron addition, that is a signature of hybridization between the Mn and boron atoms. However, the value grows with increasing T_C up to 390 K, which is the maximum value in this system. Furthermore, μ_{eff} is comparable to the saturation moment in Figure 6a. These facts suggest that the hybridization would be rather weak due to the wide space of the octahedral cavity and/or the rather low occupancy derived from being born at the octahedral site (e.g., 12.5% at x = 0.125). In the latter case, a Mn atom near the boron atom possesses a reduced magnetic moment and that with no neighboring boron atom would show an enhanced moment. Above x = 0.148, both T_C and μ_{eff} are reduced, which designates the dominating orbital hybridization between Mn and boron atoms, which is also consistent with the small change in the unit cell volume.

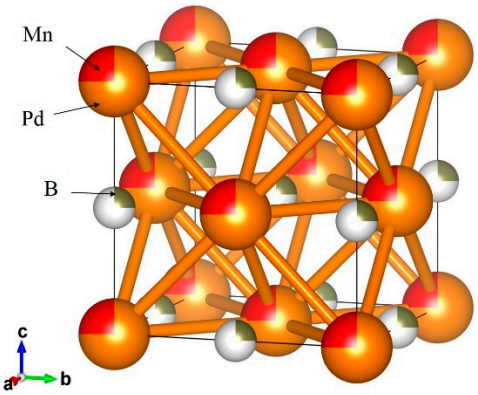

Figure 5. Crystal structure of $Pd_{0.75}Mn_{0.25}B_x$. The solid line represents the unit cell.

Table 2. Lattice parameter, unit cell volume, μ_{eff}, θ and T_C of $Pd_{0.75}Mn_{0.25}B_x$.

x	*a* (Å)	*V* (Å^3)	μ_{eff} (μ_B/Mn)	θ (K)	T_C (K)
0	3.909	59.7	4.85	−94	-
0.015	3.916	60.1	2.01	218	325
0.055	3.925	60.5	2.84	333	340
0.070	3.936	61.0	3.31	355	339
0.105	3.988	63.4	3.09	384	374
0.125	4.008	64.4	3.40	394	390
0.148	4.026	65.3	3.72	313	330
0.155	4.031	65.5	1.23	291	252
0.168	4.020	65.0	1.26	296	256

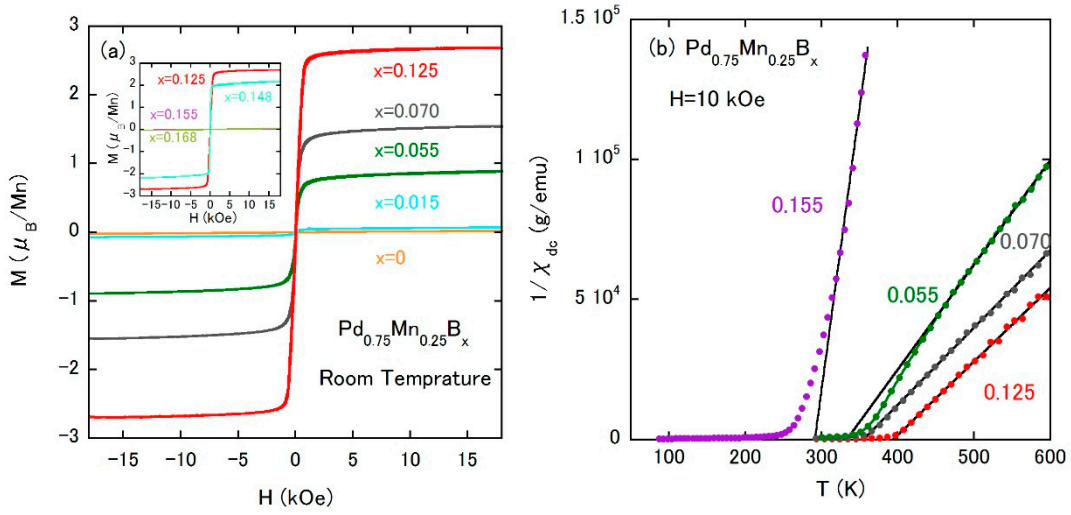

Figure 6. (**a**) Isothermal magnetization curves of $Pd_{0.75}Mn_{0.25}B_x$ at room temperature. Reproduced with permission from [49]; (**b**) temperature dependences of the inverse χ_{dc} of $Pd_{0.75}Mn_{0.25}B_x$. The external field is 10 kOe.

The magnetic phase diagram is constructed as shown in Figure 7a,b. At lower x, a coexistence of the fcc phase and the ordered derivative phase ($AuCu_3$) of fcc occurs [48,49]. The latter phase is responsible for another magnetic ordering at T_M [49]. The spin-glass state survives under the emergence of FM state, and both ordering temperatures seem to compete with each other. Therefore, this system is considered to be the typical Mn-based compound presenting the additional formation of the FM state, coexisting with the spin-glass state of Mn atoms at low temperatures. Figure 7c displays the relationship between the T_C and the unit cell volume. The vertical blue line is drawn at the volume of the parent compound showing only the spin-glass state. A linear correlation between the T_C and the unit cell volume in the region of V = 60–64 Å^3 indicates a T_C higher than 300 K even at the blue line, which means a possible abrupt birth of FM exchange coupling.

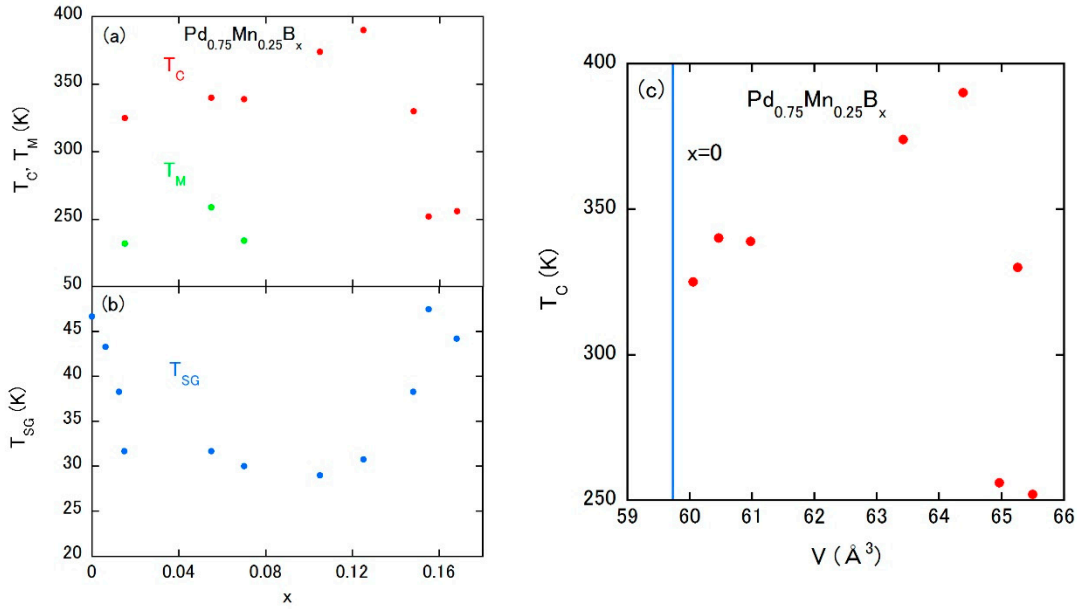

Figure 7. (**a**,**b**) Magnetic phase diagram of $Pd_{0.75}Mn_{0.25}B_x$; (**c**) T_C vs. V plot of $Pd_{0.75}Mn_{0.25}B_x$.

We remarked on the transport properties of $Pd_{0.75}Mn_{0.25}B_x$. Figure 8 shows the temperature dependences of electrical resistivity, which highlight the rather large temperature dependence

below T_C even in the disordered alloy. Considering that the spin-glass parent compound shows a weak temperature dependence, the FM interaction might produce some coherence effect on the electrical conductivity.

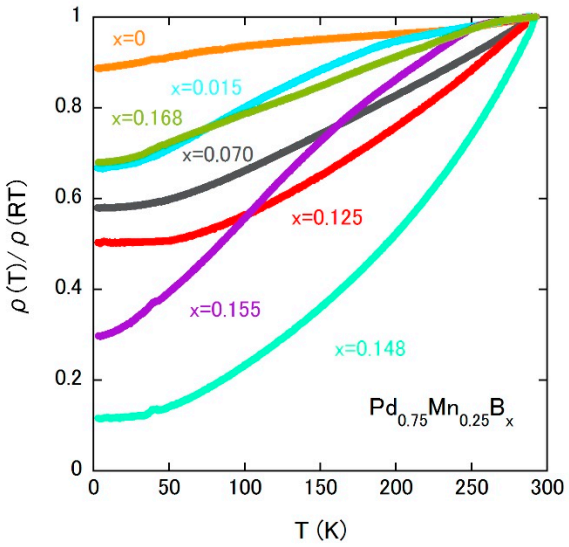

Figure 8. Temperature dependences of the electrical resistivity of $Pd_{0.75}Mn_{0.25}B_x$.

3.6. Boron-Added $Sm_2Mn_8Al_9$

$Sm_2Mn_8Al_9$ is isostructural to $R_2Fe_{17}N_x$, as mentioned in Section 2.1, and allows the interstitial B atoms at the 9*e* site (see Figure 9) [51]. In the present case, Mn and Al atoms randomly occupy the Zn sites of hexagonal Th_2Zn_{17}-type structure (space group: $R\bar{3}m$, No. 166). There is only one Wyckoff position 6*c* for Sm atoms, but Mn and Al atoms have four Wyckoff positions 6*c*, 9*d*, 18*f* and 18*h*, which are tentatively represented by Mn1, Mn2, Mn3 and Mn4, respectively, in Figure 9. The boron concentration dependences of lattice parameters and unit cell volume for $Sm_2Mn_8Al_9B_x$, determined with the help of the Rietveld refinement program [52], are listed in Table 3. The solubility limit would be x ~ 1. $\Delta V/V$ at x ≥ 0.1 is much smaller than that of $Pd_{0.75}Mn_{0.25}B_x$, which suggests the stronger orbital hybridization between Mn and boron atoms in $Sm_2Mn_8Al_9B_x$ (see also Section 2.4). We note here that the nearest neighbor atoms of boron are Mn3 and Mn4, which amount to 71% of all Mn atoms (see also Figure 9). This may lead to a large increase in hybridization under a small variation of volume by the interstitial atoms.

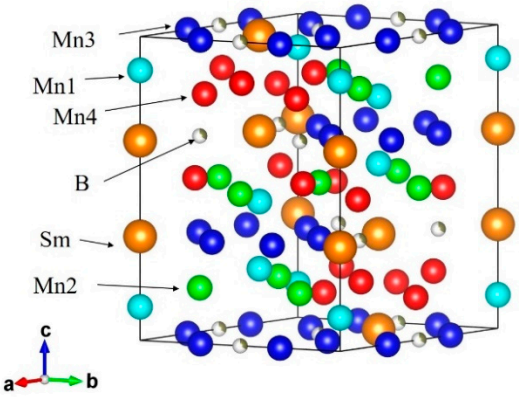

Figure 9. Crystal structure of $Sm_2Mn_8Al_9B_x$; the solid line represents the unit cell.

Table 3. Lattice parameter, unit cell volume, μ_{eff}, θ and T_C due to Mn moments of $Sm_2Mn_8Al_9B_x$. Assuming that a negligible contribution of the Sm magnetic moment is usually smaller than the Mn moment value, μ_{eff} is calculated.

x	*a* (Å)	*c* (Å)	*V* (Å^3)	μ_{eff} (μ_B/Mn)	θ (K)	T_C due to Mn (K)
0	8.970	13.109	913.5	2.89	−212	-
0.1	8.958	13.091	909.7	2.91	15	415(20)
0.5	8.958	13.093	910.0	1.34	443	408(10)
0.75	8.966	13.100	912.0	1.84	453	404(5)
1	8.975	13.112	914.6	0.98	489	437

The isothermal magnetization curves are measured at room temperature as shown in Figure 10a, which have revealed the abrupt emergence of ferromagnetism at even a small amount of boron atoms. The temperature dependences of $1/\chi_{dc}$ demonstrate that boron-added samples follow the Curie–Weiss law above T_C (see the solid lines in Figure 10b). $Sm_2Mn_8Al_9$ shows a FM behavior below approximately 100 K. Taking into account that the La-counterpart does not show a magnetic ordering at that temperature (see the ac magnetization χ_{ac} results in the inset of Figure 10b), the low-temperature magnetic transition in the parent compound is due to Sm ions. The μ_{eff} and Weiss temperature of each sample are summarized in Table 3. As x is increased, μ_{eff} is rapidly reduced, which is indicative of strong orbital hybridization, which is also supported by the weak x dependence of the unit cell volume. It is to be pointed out that the paramagnetic Mn moment abruptly forms the FM state at room temperature even when the density of boron atoms is substantially low. Under a strong orbital hybridization between Mn and boron atoms, the lattice expansion might not be essential for the formation of FM coupling at room temperature.

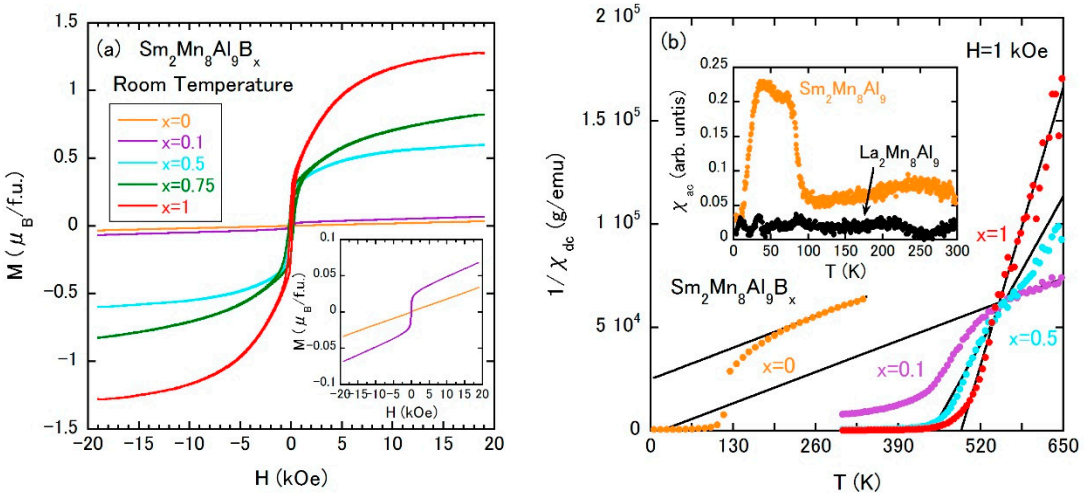

Figure 10. (**a**) Isothermal magnetization curves of $Sm_2Mn_8Al_9B_x$ at room temperature; (**b**) temperature dependences of the inverse χ_{dc} of $Sm_2Mn_8Al_9B_x$. The external field is 1 kOe, the inset is the temperature dependences of χ_{ac} of $Sm_2Mn_8Al_9$ and $La_2Mn_8Al_9$.

The magnetic properties of $Sm_2Mn_8Al_9B_x$ are summarized as a magnetic phase diagram in Figure 11a. The χ_{ac} (T) measurements indicate the survival of magnetic ordering due to Sm ions at approximately 85 K, which is independent of the room temperature FM state and seems to disappear at x = 1. The high-temperature T_C due to Mn atoms shows a shallow minimum at x = 0.75. The inset of Figure 11a is the high-temperature T_C vs. V plot, in which V at x = 0 is denoted by the vertical blue line as in Figure 7c. The observation of room temperature ferromagnetism at both sides of the vertical line strongly suggests that the birth of room temperature FM coupling between Mn atoms is

not related to the volume change. The effect of volume change, as studied well in rare-earth Fe-based magnets, is triggered by the appearance of the FM state due to Mn atoms.

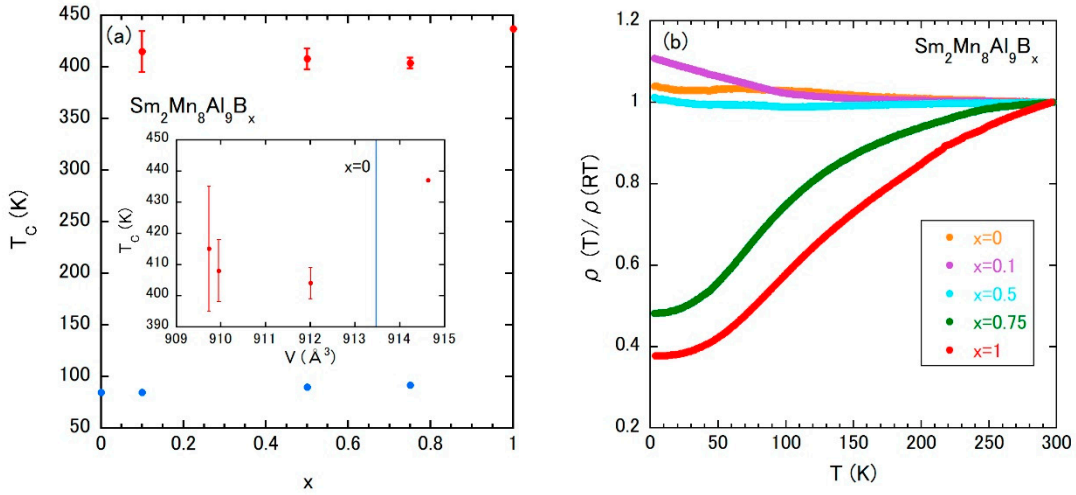

Figure 11. (**a**) Magnetic phase diagram of $Sm_2Mn_8Al_9B_x$; the inset is T_C vs. V plot of $Sm_2Mn_8Al_9B_x$; and (**b**) temperature dependences of electrical resistivity of $Sm_2Mn_8Al_9B_x$.

The temperature dependence of ρ exhibits a drastic change as shown in Figure 11b. The carriers would show a localized nature up to x = 0.5, however, metallic behavior is observed above x = 0.75. The localized behavior is also reported in isostructural Mn compounds [53] such as $Gd_2Mn_xAl_{17-x}$ and $Tb_2Mn_xAl_{17-x}$. The shift to the itinerant Mn moment with increasing x and/or some coherence effect of the FM Mn-moment observed in $Pd_{0.75}Mn_{0.25}B_x$ would be responsible for the metallic temperature dependence.

3.7. Brief Summary of Mn-Based Compounds

As in the rare-earth Fe-based compounds, the interstitial atoms give rise to the enhancement of FM interaction in the weak hybridization regime leading to the appearance of room temperature ferromagnetism. However, the Mn compounds surveyed above manifest the change or additional formation of magnetism by the interstitial atoms, while many rare-earth Fe-based parent compounds are already ferromagnets. The change from paramagnetic to FM state is observed in hydrogen-absorbed Th_6Mn_{23}, hydrogen-absorbed YMn_2 or $Sm_2Mn_8Al_9B_x$. The result of $Mn_5Si_3C_x$ thin film may be a rare example of change from the AFM to FM state by the interstitial atoms. In $Pd_{0.75}Mn_{0.25}B_x$, the room temperature ferromagnetism is induced by a slight addition of boron, while the low-temperature magnetic ground state of the parent compound is unchanged. This can be regarded as an example of the additional formation of magnetism by interstitial atoms. It should be noted that, in some cases, the change or additional formation of a magnetic state seems to abruptly occur, which is valuable for future research. We note here that the magnetic structures have been divided into FM and AFM, although some compounds may show a more complicated state such as canted AFM, and spiral AFM. In the future, discussion taking into account a more microscopic mechanism of the magnetic ordering would be necessary.

We add the comment on Mn-based Heusler compounds, which show a rich variety of physical properties such as the topological Hall effect, shape-memory and so on [54–56]. While many Mn-based Heusler compounds show ferromagnetism, a Heusler compound, allowing interstitial atoms, has not been reported to our knowledge.

3.8. Candidate Showing a Change in Magnetism by Interstitial Atoms

Mn compounds may be a superior platform to examine the change in the magnetic state or the additional formation of new magnetic coupling by interstitial atoms. We noted that, in some cases, the change to FM state or the additional formation of the FM state would occur irrespectively of interstitial atom-induced volume change. Notwithstanding, hereafter, we continue to discuss, based on the unit cell volume, because the results of $Mn_5Si_3C_x$, $Pd_{0.75}Mn_{0.25}B_x$ and $Sm_2Mn_8Al_9B_x$ are not well analyzed systematically by comparing several compounds with the same crystal structure. In other words, the magnetic ordering temperature vs. unit cell volume plot as shown in Figure 2 could not be constructed due to the absence of well investigated other Mn compounds in these crystal structures. Therefore, at the present stage, we believe that it is still valuable to survey the magnetic structures of compounds using the unit cell volumes. In this subsection, especially bearing a change in magnetism by interstitial atoms in mind, we seek a qualifying Mn compound using the magnetic ordering temperature vs. a unit cell volume plot. We selected the crystal structures allowing the site occupation of interstitial atoms: Ni_3Sn, $ThMn_{12}$, Fe_2P, Ni_2In, LiAlSi, TiNiSi, AuCu and Cu_2Sb-type structures.

3.8.1. Ni_3Sn-Type Structure

This hexagonal structure ($P6_3/mmc$, No. 194) is recently attractive as a topological AFM substance [20] represented by Mn_3Sn. All Ni_3Sn-type compounds displayed in Figure 12a possess only one crystallographic 6*h* site for the Mn atom. As seen in Figure 12a, only the AFM state has been observed and a change to FM state would be difficult.

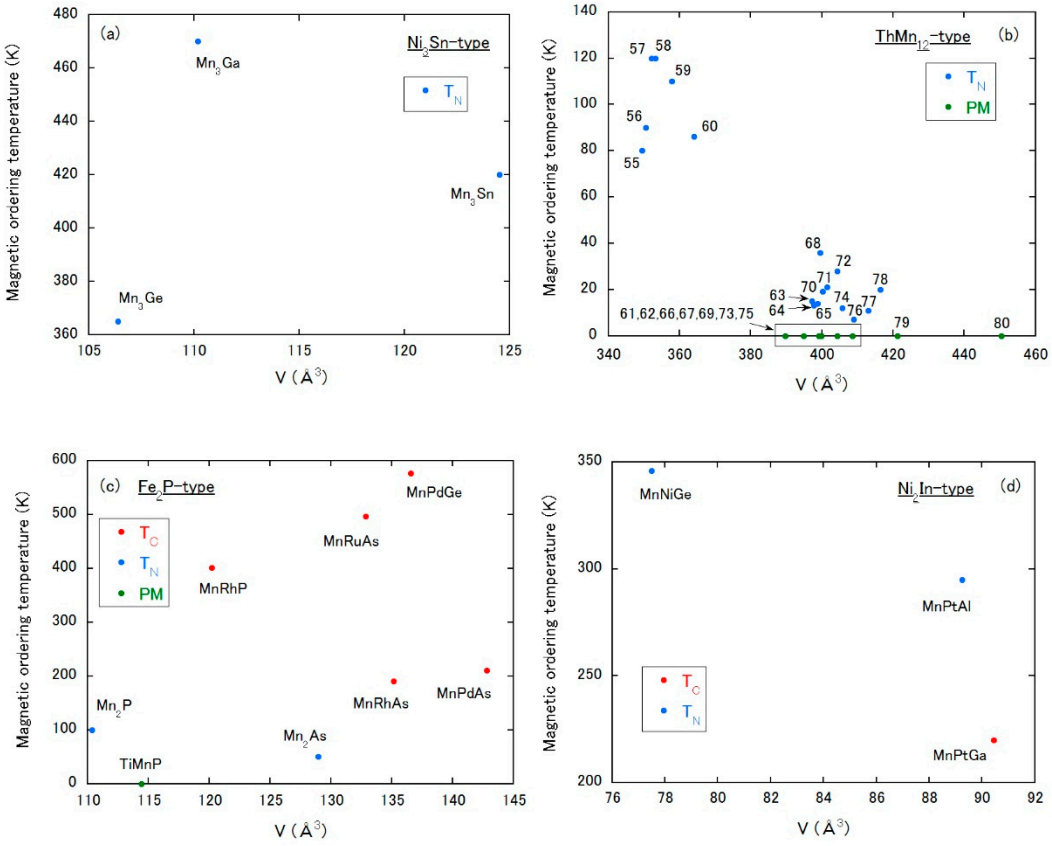

Figure 12. Magnetic ordering temperature vs. unit cell volume plot of Mn-based compounds with (**a**) Ni_3Sn-type, (**b**) $ThMn_{12}$-type, (**c**) Fe_2P-type and (**d**) Ni_2In-type, respectively. PM means a paramagnetic state down to low temperatures. The numbers in (**b**) correspond to those in Table 4.

3.8.2. $ThMn_{12}$-Type Structure

The tetragonal $ThMn_{12}$-type structure ($I4/mmm$, No. 139) is well studied in rare-earth Fe-based compounds (see Section 2.2). In the Mn compounds with this structure, Mn atoms occupy the 8*f*, 8*i*, 8*j* sites. As shown in Figure 12b, the magnetic properties are dominated by the AFM state. We note that, except for compounds No. 55–60, the AFM orderings of compounds containing rare-earth elements are triggered by the magnetic moments of rare-earth, and Mn atoms do not carry moments. Basically, with increasing volume, T_N tends to be suppressed. In this class of compounds, a change from AFM to a paramagnetic state of Mn atoms by interstitial atoms may be anticipated.

3.8.3. Fe_2P-Type Structure

The compounds with the hexagonal Fe_2P-type structure ($P\bar{6}2m$, No. 189) displayed in Figure 12c possess the 3*g* site for the Mn atom, except Mn_2P and Mn_2As, in which there exists the 3*g* and 3*f* sites for Mn atoms. Figure 12c indicates a possible crossover from paramagnetic to FM state across the volume of approximately 115–120 $Å^3$ for compounds with only the 3*g* Mn site.

3.8.4. Ni_2In-Type Structure

The Ni_2In-type structure is hexagonal with the space group of $P6_3/mmc$ (No. 194). Each compound has only one Mn site of the 2*a*. In this structure, T_N at a smaller volume tends to be suppressed as the volume is expanded and seems to transform to T_C with further increasing volume (Figure 12d). The compounds with the $ThMn_{12}$-, the Fe_2P- or the Ni_2In-type structure may be good candidates for examining a change in magnetic state by interstitial atoms as a function of the unit cell volume.

3.8.5. LiAlSi-Type Structure

This structure is cubic with the space group of $F\bar{4}3m$ (No. 216). Each compound in Figure 13a possesses one Mn site with the 4*a*, 4*b* or 4*c*, depending on the literature. The magnetic ordering types of the cubic compounds would be classified by the VEC, which is different from the results of Figure 12a–d. The VEC values are denoted under the chemical formulae in Figure 13a. Except for the compounds with VEC = 7.7 showing the AFM state, all compounds undergo FM as one. In FM compounds, T_C tends to increase as the VEC is increased. If interstitial atoms change VEC from 7.33 to 7.7, a change between FM and AFM states might be possible, which may be a new phenomenon induced by interstitial atoms.

Table 4. Structural and magnetic properties of Mn-based compounds. T_{order} is the magnetic ordering temperature. FM, AFM and PM mean ferromagnetic, antiferromagnetic and paramagnetic, respectively. Data are from the references listed in the table.

No.	Compound	Structure Type	*a* (Å)	*b* (Å)	*c* (Å)	*V*(Å^3)	T_{order} (K)	Type	Ref.
1	Lu_6Mn_{23}	Th_6Mn_{23}	12.187	12.187	12.187	1810.0	398	FM	[57]
2	Yb_6Mn_{23}	Th_6Mn_{23}	12.189	12.189	12.189	1810.9	406	FM	[58]
3	Tm_6Mn_{23}	Th_6Mn_{23}	12.226	12.226	12.226	1827.5	411	FM	[57]
4	Er_6Mn_{23}	Th_6Mn_{23}	12.275	12.275	12.275	1849.5	430	FM	[57]
5	Ho_6Mn_{23}	Th_6Mn_{23}	12.324	12.324	12.324	1871.8	445	FM	[57]
6	Dy_6Mn_{23}	Th_6Mn_{23}	12.361	12.361	12.361	1888.7	447	FM	[57]
7	Tb_6Mn_{23}	Th_6Mn_{23}	12.396	12.396	12.396	1904.8	457	FM	[57]
8	Y_6Mn_{23}	Th_6Mn_{23}	12.438	12.438	12.438	1924.2	500	FM	[59]
9	$Gd_6Mn_{23}H_{24}$	Th_6Mn_{23}	12.515	12.515	12.515	1960.2	260	FM	[60]
10	Th_6Mn_{23}	Th_6Mn_{23}	12.523	12.523	12.523	1963.9	0	PM	[59]
11	Sm_6Mn_{23}	Th_6Mn_{23}	12.558	12.558	12.558	1980.4	456	FM	[57]
12	Gd_6Mn_{23}	Th_6Mn_{23}	12.578	12.578	12.578	1989.9	489	FM	[57]
13	Nd_6Mn_{23}	Th_6Mn_{23}	12.657	12.657	12.657	2027.6	441	FM	[57]

Table 4. *Cont.*

No.	Compound	Structure Type	*a* (Å)	*b* (Å)	*c* (Å)	*V*(Å^3)	T_{order} (K)	Type	Ref.
14	$Y_6Mn_{23}H_{23}$	Th_6Mn_{23}	12.805	12.805	12.805	2099.6	180	AFM	[61]
15	$Th_6Mn_{23}D_{16}$	Th_6Mn_{23}	12.922	12.922	12.922	2157.7	329	FM	[62]
16	$Gd_{12}Mn_{45}H_{43}$	Th_6Mn_{23}	12.97	12.97	12.97	2181.8	180	FM	[63]
17	$Tb_6Mn_{23}H_{23}$	Th_6Mn_{23}	13.017	13.017	13.017	2205.6	220	FM	[64]
18	$Sm_6Mn_{23}H_{24}$	Th_6Mn_{23}	13.04	13.04	13.04	2217.3	230	FM	[60]
19	$Nd_6Mn_{23}H_{24}$	Th_6Mn_{23}	13.237	13.237	13.237	2319.4	220	FM	[60]
20	$Th_6Mn_{23}H_{30}$	Th_6Mn_{23}	13.259	13.259	13.259	2330.9	329	FM	[59]
21	YMn_2Si_2	$ThCr_2Si_2$	3.924	3.924	10.457	161.0	463	AFM	[65]
22	$LaMn_2Si_2$	$ThCr_2Si_2$	4.1151	4.1151	10.612	179.7	305	FM	[65]
23	$CeMn_2Si_2$	$ThCr_2Si_2$	3.99	3.99	10.51	167.3	377	AFM	[65]
24	$PrMn_2Si_2$	$ThCr_2Si_2$	4.03	4.03	10.559	171.5	350	AFM	[65]
25	$NdMn_2Si_2$	$ThCr_2Si_2$	4.063	4.063	10.522	173.7	368	AFM	[65]
26	$SmMn_2Si_2$	$ThCr_2Si_2$	3.975	3.975	10.52	166.2	400	AFM	[65]
27	$EuMn_2Si_2$	$ThCr_2Si_2$	3.966	3.966	10.387	163.4	391	AFM	[66]
28	$GdMn_2Si_2$	$ThCr_2Si_2$	3.948	3.948	10.468	163.2	454	AFM	[65]
29	$TbMn_2Si_2$	$ThCr_2Si_2$	3.931	3.931	10.456	161.6	504	AFM	[65]
30	$DyMn_2Si_2$	$ThCr_2Si_2$	3.915	3.915	10.44	160.0	477	AFM	[65]
31	$HoMn_2Si_2$	$ThCr_2Si_2$	3.931	3.931	10.412	160.9	455	AFM	[65]
32	$ErMn_2Si_2$	$ThCr_2Si_2$	3.905	3.905	10.42	158.9	518	AFM	[65]
33	$TmMn_2Si_2$	$ThCr_2Si_2$	3.887	3.887	10.398	157.1	500	AFM	[65]
34	$YbMn_2Si_2$	$ThCr_2Si_2$	3.877	3.877	10.391	156.2	512	AFM	[65]
35	$LuMn_2Si_2$	$ThCr_2Si_2$	3.873	3.873	10.37	155.6	468	AFM	[65]
36	YMn_2Ge_2	$ThCr_2Si_2$	4.0516	4.0516	10.854	178.2	395	AFM	[65]
37	$LaMn_2Ge_2$	$ThCr_2Si_2$	4.195	4.195	11.022	194.0	309	FM	[65]
38	$CeMn_2Ge_2$	$ThCr_2Si_2$	4.144	4.144	10.97	188.4	325	FM	[65]
39	$PrMn_2Ge_2$	$ThCr_2Si_2$	4.123	4.123	10.929	185.8	336	FM	[65]
40	$NdMn_2Ge_2$	$ThCr_2Si_2$	4.1022	4.1022	10.909	183.6	334	FM	[65]
41	$SmMn_2Ge_2$	$ThCr_2Si_2$	4.062	4.062	10.896	179.8	350	FM	[65]
42	$GdMn_2Ge_2$	$ThCr_2Si_2$	4.029	4.029	10.895	176.9	368	AFM	[65]
43	$TbMn_2Ge_2$	$ThCr_2Si_2$	4.006	4.006	10.875	174.5	418	AFM	[65]
44	$DyMn_2Ge_2$	$ThCr_2Si_2$	3.989	3.989	10.863	172.9	386	AFM	[65]
45	$HoMn_2Ge_2$	$ThCr_2Si_2$	3.977	3.977	10.847	171.6	404	AFM	[65]
46	$ErMn_2Ge_2$	$ThCr_2Si_2$	3.948	3.948	10.791	168.2	395	AFM	[65]
47	$YbMn_2Ge_2$	$ThCr_2Si_2$	4.067	4.067	10.871	179.8	341	AFM	[65]
48	$ThMn_2Si_2$	$ThCr_2Si_2$	4.0225	4.0225	10.475	169.5	486	AFM	[65]
49	UMn_2Si_2	$ThCr_2Si_2$	3.922	3.922	10.284	158.2	377	FM	[67]
50	$ThMn_2Ge_2$	$ThCr_2Si_2$	4.084	4.084	10.93	182.3	400	AFM	[65]
51	UMn_2Ge_2	$ThCr_2Si_2$	4.012	4.012	10.803	173.9	390	FM	[67]
52	Mn_3Ge	Ni_3Sn	5.338	5.338	4.312	106.4	365	AFM	[68]
53	Mn_3Ga	Ni_3Sn	5.404	5.404	4.357	110.2	470	AFM	[69]
54	Mn_3Sn	Ni_3Sn	5.64	5.64	4.52	124.5	420	AFM	[20]
55	$ErMn_{12}$	$ThMn_{12}$	8.5719	8.5719	4.7553	349.4	80	AFM	[70]
56	$HoMn_{12}$	$ThMn_{12}$	8.5817	8.5817	4.7592	350.5	90	AFM	[71]
57	YMn_{12}	$ThMn_{12}$	8.597	8.597	4.7637	352.1	120	AFM	[72]
58	$TbMn_{12}$	$ThMn_{12}$	8.6076	8.6076	4.7666	353.2	120	AFM	[73]
59	$DyMn_{12}$	$ThMn_{12}$	8.67	8.67	4.76	357.8	110	AFM	[74]
60	$GdMn_{12}$	$ThMn_{12}$	8.673	8.673	4.839	364.0	86	AFM	[74]
61	$ScMn_4Al_8$	$ThMn_{12}$	8.7734	8.7734	5.0629	389.7	0	PM	[75]
62	$LuMn_4Al_8$	$ThMn_{12}$	8.814	8.814	5.083	394.9	0	PM	[75]
63	$ErMn_4Al_8$	$ThMn_{12}$	8.829	8.829	5.096	397.2	15	AFM	[76]
64	$TmMn_4Al_8$	$ThMn_{12}$	8.848	8.848	5.08	397.7	13	AFM	[76]
65	$HoMn_4Al_8$	$ThMn_{12}$	8.845	8.845	5.097	398.8	14	AFM	[76]
66	UMn_4Al_8	$ThMn_{12}$	8.8474	8.8474	5.0993	399.2	0	PM	[77]
67	YMn_4Al_8	$ThMn_{12}$	8.86	8.86	5.09	399.6	0	PM	[76]
68	$GdMn_6Al_6$	$ThMn_{12}$	8.845	8.845	5.108	399.6	36	AFM	[78]
69	$YbMn_4Al_8$	$ThMn_{12}$	8.854	8.854	5.102	400.0	0	PM	[76]

Table 4. *Cont.*

No.	Compound	Structure Type	*a* (Å)	*b* (Å)	*c* (Å)	*V*(Å^3)	T_{order} (K)	Type	Ref.
70	$DyMn_4Al_8$	$ThMn_{12}$	8.849	8.849	5.112	400.3	19	AFM	[76]
71	$TbMn_4Al_8$	$ThMn_{12}$	8.865	8.865	5.108	401.4	21	AFM	[76]
72	$GdMn_4Al_8$	$ThMn_{12}$	8.887	8.887	5.119	404.3	28	AFM	[76]
73	$TbMn_{4.04}Al_{7.96}$	$ThMn_{12}$	8.8885	8.8885	5.1179	404.3	0	PM	[79]
74	$SmMn_4Al_8$	$ThMn_{12}$	8.902	8.902	5.12	405.7	12	AFM	[76]
75	$CeMn_4Al_8$	$ThMn_{12}$	8.89	8.89	5.17	408.6	0	PM	[76]
76	$NdMn_4Al_8$	$ThMn_{12}$	8.925	8.925	5.133	408.9	7	AFM	[76]
77	$PrMn_4Al_8$	$ThMn_{12}$	8.962	8.962	5.143	413.1	11	AFM	[76]
78	$EuMn_4Al_8$	$ThMn_{12}$	8.982	8.982	5.161	416.4	20	AFM	[76]
79	$LaMn_4Al_8$	$ThMn_{12}$	9.031	9.031	5.166	421.3	0	PM	[76]
80	$ThMn_4Al_8$	$ThMn_{12}$	8.937	8.937	5.639	450.4	0	PM	[80]
81	Mn_2P	Fe_2P	6.074	6.074	3.454	110.4	100	AFM	[81, 82]
82	TiMnP	Fe_2P	6.188	6.188	3.451	114.4	0	PM	[83]
83	MnRhP	Fe_2P	6.226	6.226	3.581	120.2	401	FM	[84]
84	Mn_2As	Fe_2P	6.3627	6.3627	3.6784	129.0	50	AFM	[85]
85	MnRuAs	Fe_2P	6.5155	6.5155	3.614	132.9	496	FM	[84]
86	MnRhAs	Fe_2P	6.482	6.482	3.714	135.1	190	FM	[86]
87	MnPdGe	Fe_2P	6.639	6.639	3.577	136.5	576	FM	[87]
88	MnPdAs	Fe_2P	6.626	6.626	3.756	142.8	210	FM	[84]
89	MnNiGe	Ni_2In	4.078	4.078	5.381	77.50	346	AFM	[88]
90	MnPtAl	Ni_2In	4.329	4.329	5.499	89.25	295	AFM	[89]
91	MnPtGa	Ni_2In	4.328	4.328	5.576	90.45	220	FM	[90]
92	NiMnSb	LiAlSi	5.928	5.928	5.928	208.3	728	FM	[91]
93	MnIrAl	LiAlSi	5.981	5.981	5.981	214.0	379	FM	[92]
94	MnCuSb	LiAlSi	6.095	6.095	6.095	226.4	55	AFM	[93]
95	MnRhSb	LiAlSi	6.142	6.142	6.142	231.7	320	FM	[93]
96	MnIrSn	LiAlSi	6.182	6.182	6.182	236.3	265	FM	[94]
97	MnPtSb	LiAlSi	6.21	6.21	6.21	239.5	585	FM	[93]
98	PdMnSb	LiAlSi	6.231	6.231	6.231	241.9	500	FM	[95]
99	MnPdTe	LiAlSi	6.2605	6.2605	6.2605	245.4	17	AFM	[96]
100	MnPtSn	LiAlSi	6.264	6.264	6.264	245.8	330	FM	[93]
101	MnAuSn	LiAlSi	6.4313	6.4312	6.4312	266.0	740	FM	[97]
102	MnRhSi	TiNiSi	6.1994	3.7968	7.1387	168.0	367	AFM	[98]
103	HfMnP	TiNiSi	6.3257	3.6298	7.409	170.1	320	FM	[99]
104	ZrMnP	TiNiSi	6.41	3.657	7.515	176.2	370	FM	[99]
105	LuMnSi	TiNiSi	6.82	3.962	7.839	211.8	255	AFM	[100]
106	UMnGe	TiNiSi	6.866	4.2594	7.3618	215.3	240	AFM	[101]
107	TbMnGe	TiNiSi	7.077	4.132	8.166	238.8	510	AFM	[102]
108	GdMnGe	TiNiSi	7.138	4.1698	8.191	243.8	490	AFM	[103]
109	MnNi	AuCu	3.69	3.69	2.609	35.52	1070	AFM	[104]
110	MnPt	AuCu	3.855	3.855	2.726	40.51	970	AFM	[104]
111	MnGa	AuCu	3.889	3.889	2.75	41.59	629	FM	[105]
112	MnRh	AuCu	3.93	3.93	2.779	42.92	0	PM	[104]
113	MnPd	AuCu	4.069	4.069	2.877	47.63	780	AFM	[104]
114	MnAl	AuCu	3.9	3.9	3.54	53.84	578	FM	[106]
115	$MnRh_2Sb$	AuCu	4.171	4.171	3.494	60.79	304	FM	[107]
116	MnAlGe	Cu_2Sb	3.914	3.914	5.933	90.89	518	FM	[108]
117	MnGaGe	Cu_2Sb	3.966	3.966	5.885	92.57	440	FM	[109]
118	MnZnSb	Cu_2Sb	4.173	4.173	6.233	108.5	310	FM	[110]
119	LiMnAs	Cu_2Sb	4.267	4.267	6.178	112.5	374	AFM	[111]
120	YMnSi	Cu_2Sb	3.978	3.978	7.152	113.2	282	FM	[112]
121	GdMnSi	Cu_2Sb	4.009	4.009	7.183	115.5	314	FM	[113]
122	NdMnSi	Cu_2Sb	4.087	4.087	7.245	121.0	175	AFM	[114]
123	CeMnSi	Cu_2Sb	4.13	4.13	7.279	124.2	240	AFM	[114]
124	CaMnSi	Cu_2Sb	4.1814	4.1814	7.1429	124.9	360	AFM	[115]

Table 4. *Cont.*

No.	Compound	Structure Type	*a* (Å)	*b* (Å)	*c* (Å)	*V*(Å^3)	T_{order} (K)	Type	Ref.
125	PrMnGe	Cu_2Sb	4.196	4.196	7.344	129.3	415	AFM	[116]
126	LaMnSi	Cu_2Sb	4.189	4.189	7.378	129.5	310	AFM	[114]
127	CaMnGe	Cu_2Sb	4.23	4.23	7.27	130.1	420	AFM	[115]
128	CeMnGe	Cu_2Sb	4.226	4.226	7.386	131.9	415	AFM	[116]
129	LaMnGe	Cu_2Sb	4.277	4.277	7.449	136.3	420	AFM	[116]
130	SrMnGe	Cu_2Sb	4.4	4.4	7.52	145.6	254	AFM	[117]
131	CaMnSn	Cu_2Sb	4.4839	4.4839	7.4988	150.8	250	AFM	[117]
132	BaMnGe	Cu_2Sb	4.5	4.5	7.92	160.4	425	AFM	[117]
133	SrMnSn	Cu_2Sb	4.662	4.662	7.749	168.4	252	AFM	[117]

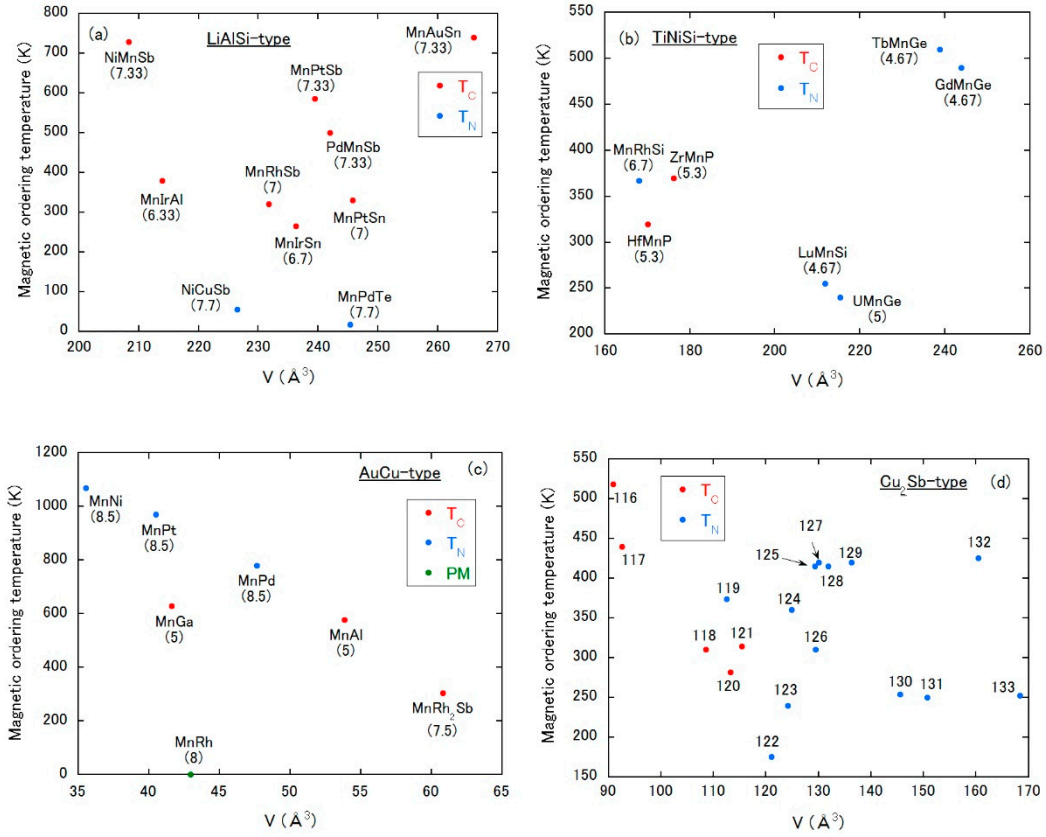

Figure 13. Magnetic ordering temperature vs. unit cell volume plot of Mn-based compounds with (**a**) LiAlSi-type, (**b**) TiNiSi-type, (**c**) AuCu-type and (**d**) Cu_2Sb-type, respectively. PM means a paramagnetic state down to low temperatures. In (**a**–**c**), valence electron count per atom (VEC) is denoted under each chemical formula. The numbers in (**d**) correspond to those in Table 4.

3.8.6. TiNiSi-Type Structure

This is the famous orthorhombic structure with the space group *Pnma* (No. 62). Mn atoms occupy the 4*c* site. As shown in Figure 13b, the border between AFM and FM states may be situated at V = 180–200 Å^3. Moreover, only the compounds accompanied by VEC = 5.3 show the FM ground state. The interstitial alloying with the change in VEC might be effective for a magnetic state change.

3.8.7. AuCu-Type Structure

The AuCu-type structure is tetragonal with the space group of *P*4/*mmm* (No. 123). Except for $MnRh_2Sb$, Mn atoms occupy two crystallographic sites called the 1*a* and 1*c* sites. In $MnRh_2Sb$, Mn sites

are reduced to the 1*a* one. As in the LiAlSi-type structure, the magnetic ordering type would be correlated with VEC; the AFM or paramagnetic state is observed for a VEC larger than 8, and the FM state for VEC = 5 or 7.5. Under a fixed VEC value, T_N systematically decreases with increasing volume, while the volume dependence of T_C is very weak for ferromagnets.

3.8.8. Cu_2Sb-Type Structure

This is the tetragonal structure (*P*4/*nmm*, No. 129), in which Mn atoms occupy the 2*a* site. Contrary to the prediction of the Bethe–Slater curve, a volume expansion favors an AFM state. The magnitude of the magnetic ordering temperature is likely suppressed by expanding the volume.

4. Rare-Earth-Based Compounds

4.1. $R_5Si_3B_x$

The Mn_5Si_3-type R_5Si_3 allows for interstitial boron atoms, which leads to volume reduction with an increasing boron concentration [118]. For the parent compound with x = 0, the AFM orderings are observed in R = Gd and Tb at T_N = 75 and 69 K, respectively. On the other hand, R = Dy and Ho show the FM orderings at T_C = 120 and 11 K, respectively. By adding boron atoms, the T_N of R = Gd and Tb are slightly reduced to 67 K in both cases, and the changes of T_C in R = Dy and Ho are also subtle; T_C remains at 120 K in R = Dy and is slightly enhanced to 15 K in R = Ho. In each compound, μ_{eff} does not so largely depend on the boron addition, which means a weak hybridization between rare earth and boron atoms.

4.2. $NdScSiC_x$

This compound crystallizes into the tetragonal La_2Sb-type structure (*I*4/*mmm*, No. 139) [119]. The interstitial carbon atoms expand the *a* axis and contract the *c* axis. The latter fact, in particular, enhances the chemical bonding between Nd and C and decreases T_C = 171 K in the parent NdScSi to 50 K at x = 0.5. Taking into account that the 4*f* orbital of a rare-earth atom is usually well localized, the drastic change in magnetic ordering temperature is unexpected as in $R_5Si_3B_x$. Thus, the large modification of T_C in this compound is very interesting.

5. Perspectives

5.1. Application of Mn-Based Magnetic Materials

The change in magnetism between FM and AFM states or the additional formation of new magnetic coupling at rather high temperatures by interstitial atoms is substantially valuable in a magnetic device integrated with both FM and AFM materials due to the easy on-demand control of magnetism in the fabrication process. At the present stage, Mn-based compounds fulfill the requirement of change or the additional formation of magnetism, while in Fe-based compounds, only improvements of FM properties are extensively investigated and the change (or the additional formation) of the magnetic state is not well explored. Focusing on the research area of the permanent magnet, a rare-earth Mn-based permanent magnet is still missing, although the MnBi-type magnets are well known. Based on the Bethe–Slater curve, Mn atoms favor the FM state with expanding Mn–Mn distance. Therefore, the density of Mn could not be so increased as in rare-earth Fe-based permanent magnets, resulting in a smaller saturation magnetization. However, there exists a large gap of *BH* energy product between the NdFeB magnets and ferrite magnets, and a rare-earth Mn-based permanent magnet may be a good candidate filling the gap [120].

5.2. Towards Further on-Demand Control of Magnetism

Further improvement of magnetic properties in the on-demand control would be achieved by another strategy such as a composition effect and carrier doping. If a metallurgical phase diagram of

a target compound possesses a homogeneity range, the magnetic ordering temperature often varies with the atomic composition. For example, the T_C of Tb_2Co_2Ga ranges rather widely from 75 to 145 K by changing the starting composition [121]. Such a composition effect is reported in other compounds [122–124] such as $Nd_3Pd_{20}Ge_6$, Tb_3Co_3Ga and $Mn_{1+x}Ga$. In many cases, the crystal structure parameters slightly change, which heavily affects the magnetic exchange interactions.

The magnetic anisotropy energy is one of the important factors in characterizing a ferromagnet. It is known that it can be tuned by doping, mainly due to the variation of the density of states near the Fermi level. The doping effect is reported in, for example, Ni_2MnGa, $SmCo_{5-x}Fe$, MnBi, $Nd_2Fe_{17}X$ (X = C or N), Ce_2AuP_3 and so on [125–129]. Taking into account the crystal symmetry, which is related to the magnetic anisotropy energy, a lower crystal symmetry with more tunable crystal parameters might be favorable.

5.3. Comments on Control of Magnetism by External Field

Another interesting control of magnetism is the manipulation of spin by external fields such as the electric field and the optical light. For example, the employment of an electric double-layer transistor has achieved a control of magnetism by weak voltage [130]. Recently, an optical change in magnetism through the Kondo effect has been reported [131]. The interstitial atoms may precisely control the magnetism so that only a small magnitude of external field is required for the device working, and the power consumption can be highly reduced.

5.4. Comments on Critical Behavior

From the fundamental viewpoint, research into critical behavior is interesting. Actually, in strongly correlated electron systems, there have been plenty of studies for seeking a quantum critical point under the suppression of magnetism [132–136]. We speculate that a formation of FM exchange coupling above room temperature would be a discontinuous phenomenon as mentioned in the results of Mn-based compounds. While it is not well investigated for rare-earth Fe-based compounds, we note that $RFe_{11}TiC_x$ and $RFe_{11}TiC_x$ show a finite change in T_C at an infinitely zero value of volume expansion depending on R species [137].

6. Summary

This review surveyed the studies of interstitial atoms in rare-earth Fe-, Mn-, rare-earth-based magnetic materials, especially focusing on the Mn-based compounds since the effect of interstitial atoms is not well investigated. The light elements would occupy the interstitial sites in the respective crystal structure, and change the unit cell volume, although the degree of change depends on the strength of orbital hybridization between the magnetic and interstitial atoms. The light elements are occasionally essential for the stabilization of the desired crystal structure. In the abundant studies of rare-earth Fe-based permanent magnets, the role of interstitial atoms seems to be restricted to the enhancements of T_C and saturated magnetization, and the change in easy magnetization direction. In several Mn-based compounds, magnetic ordering temperature and the magnetization also tends to be increased with the increasing density of interstitial atoms after the appearance of FM states. However, it is peculiar for the Mn-based compounds that the change or additional formation of magnetism by interstitial atoms is possible: the change from the AFM (paramagnetic) to FM state or the additional formation of the FM state coexisting with the ground state of Mn atoms in the parent compound. Furthermore, the FM exchange coupling would abruptly emerge under a slight addition of interstitial elements, and this is an important research topic for a deep understanding of interstitial atom engineering. The candidates of Mn-based compounds, possibly showing the change in magnetism by interstitial atoms, are briefly discussed. We note that not only the unit cell volume but also the VEC should be taken into account to design the change in magnetism. The change between AFM and FM states by just controlling the number of interstitial atoms is a very promising elemental technology for making highly functional magnetic devices integrated with both FM and AFM materials without a large lattice mismatch.

Author Contributions: Conceptualization, J.K., N.S. and M.T.; methodology, J.K., N.S. and M.T.; formal analysis, J.K., K.S., T.H. and F.H.; writing—original draft preparation, J.K.; writing—review and editing, J.K., N.S. and M.T. All authors have read and agreed to the published version of the manuscript.

Funding: This research received no external funding.

Acknowledgments: J.K. is grateful for the support provided by Comprehensive Research Organization of Fukuoka Institute of Technology.

Conflicts of Interest: The authors declare no conflict of interest.

References

1. Goldschmidt, H.J. *Interstitial Alloys*; Butterworths: London, UK, 1967.
2. Grandjean, F.; Long, G.J.; Buschow, K.H.J. *Interstitial Intermetallic Alloys*; Kluwer Academic Publishers: Dordrecht, The Netherlands, 1995.
3. Yang, Y.; Yang, J.; Han, J.; Wang, C.; Liu, S.; Du, H. Researh and Development of Interstitial Compounds. *IEEE Trans. Magn.* **2015**, *51*, 2103806. [CrossRef]
4. Nieves, P.; Arapan, S.; Maudes-Raedo, J.; Marticorena-Sánchez, R.; Del Brío, N.L.; Kovacs, A.; Echevarria-Bonet, C.; Salazar, D.; Weischenberg, J.; Zhang, H.; et al. Database of novel magnetic materials for high-performance permanent magnet development. *Comput. Mater. Sci.* **2019**, *168*, 188–202. [CrossRef]
5. Coey, J.M.D. Perspective and Prospects for Rare Earth Permanent Magnets. *Engineering* **2020**, *6*, 119–131. [CrossRef]
6. Hadjipanayis, G.C.; Gabay, A.M.; Schönhöbel, A.M.; Martín-Cid, A.; Barandiaran, J.M.; Niarchos, D. $ThMn_{12}$-Type Alloys for Permanent Magnets. *Engineering* **2020**, *6*, 141–147. [CrossRef]
7. Slater, J.C. Cohesion in Monovalent Metals. *Phys. Rev.* **1930**, *35*, 509–529. [CrossRef]
8. Slater, J.C. Atomic Shielding Constants. *Phys. Rev.* **1930**, *36*, 57–64. [CrossRef]
9. Sommerfeld, A.; Bethe, H. *Handbuch der Physik*; Springer: Berlin, Germany, 1933; Volume 24, p. 595.
10. Cardias, R.; Szilva, A.; Bergman, A.; Marco, I.D.; Katsnelson, M.I.; Lichtenstein, A.I.; Nordström, L.; Klautau, A.B.; Eriksson, O.; Kvashnin, Y.O. The Bethe-Slater curve revisited; new insights from electronic structure theory. *Sci. Rep.* **2017**, *7*, 4058. [CrossRef]
11. Givord, D.; Lemaire, R. Magnetic Transition and Anomalous Thermal Expansion in R_2Fe_{17} Compounds. *IEEE Trans. Magn.* **1970**, *MAG-10*, 109–113.
12. Palstra, T.T.M.; Nieuwenhuys, G.J.; Mydosh, J.A.; Buschow, K.H.J. Mictomagnetic, ferromagnetic, and antiferromagnetic transitions in $La(Fe_xAl_{1-x})_{13}$ intermetallic compounds. *Phys. Rev. B* **1985**, *31*, 4622–4632. [CrossRef]
13. Kitagawa, J.; Yakabe, G.; Nakayama, A.; Nishizaki, T.; Tsubota, M. Competition between ferromagnetic and antiferromagnetic states in $Al_{8.5-x}Fe_{23}Ge_{12.5+x}$ ($0 \leq x \leq 3$). *J. Solid State Chem.* **2020**, *284*, 121188. [CrossRef]
14. Chen, D.; Gondō, Y. Temperature Dependence of the Magneto-Optic Effect and Resonance Phenomena in Oriented MnBi Films. *J. Appl. Phys.* **1964**, *35*, 1024–1025. [CrossRef]
15. Park, J.H.; Hong, Y.K.; Bae, S.; Lee, J.J.; Jalli, J.; Abo, G.S.; Neveu, N.; Kim, S.G.; Choi, C.J.; Lee, J.G. Saturation magnetization and crystalline anisotropy calculations for MnAl permanent magnet. *J. Appl. Phys.* **2010**, *107*, 09A731. [CrossRef]
16. Gabay, A.M.; Hadjipanayis, G.C.; Cui, J. New anisotropic MnBi permanent magnets by field-annealing of compacted melt-spun alloys modified with Mg and Sb. *J. Magn. Magn. Mater.* **2020**, *495*, 165860. [CrossRef]
17. Xiang, Z.; Xu, C.; Wang, T.; Song, Y.; Yang, H.; Lu, W. Enhanced magnetization and energy product in isotropic nanocrystalline $Mn_{55}Al_{45}$ alloys with boron doping. *Intermetallics* **2018**, *101*, 13–17. [CrossRef]
18. Zhao, S.; Wu, Y.; Zhang, C.; Wang, J.; Fu, Z.; Zhang, R.; Jiang, C. Stabilization of τ-phase in carbon-doped MnAl magnetic alloys. *J. Alloy. Compd.* **2018**, *755*, 257–264. [CrossRef]
19. Jonietz, F.; Mühlbauer, S.; Pfleiderer, C.; Neubauer, A.; Münzer, W.; Bauer, A.; Adams, T.; Georgii, R.; Böni, P.; Duine, R.A.; et al. Spin Transfer Torques in MnSi at Ultralow Current Densities. *Science* **2010**, *330*, 1648–1651. [CrossRef]
20. Nakatsuji, S.; Kiyohara, N.; Higo, T. Large anomalous Hall effect in a non-collinear antiferromagnet at room temperature. *Nature* **2015**, *527*, 212–215. [CrossRef]
21. Sun, H.; Coey, J.M.D.; Otani, Y.; Hurley, D.P.F. Magnetic properties of a new series of rare-earth iron nitrides: $R_2Fe_{17}N_y$ (y approximately 2.6). *J. Phys. Condens. Matter* **1990**, *2*, 6465–6470. [CrossRef]

22. Mukai, T.; Fujimoto, T. Kerr microscopy observation of nitrogenated Sm_2Fe_{17} intermetallic compounds. *J. Magn. Magn. Mater.* **1992**, *103*, 165–173. [CrossRef]
23. Coey, J.M.D. Novel Permanent Magnetic Materials. *Phys. Scr.* **1991**, *T39*, 21–28. [CrossRef]
24. Wei, Y.-N.; Sun, K.; Fen, Y.-B.; Zhang, J.-X.; Hu, B.-P.; Wang, Y.-Z.; Rao, X.-L.; Liu, G.-C. Structural and intrinsic magnetic properties of $Sm_2Fe_{17}N_y$ (y = 2 − 8). *J. Alloy. Compd.* **1993**, *194*, 9–12. [CrossRef]
25. Coey, J.M.D.; Hurley, D.P.F. New interstitial rare-earth iron intermetallics produced by gas phase reaction. *J. Magn. Magn. Mater.* **1992**, *104–107*, 1098–1101. [CrossRef]
26. Christodoulou, C.N.; Takeshita, T. Interstitial carbonation of the Sm_2Fe_{17} phase by reaction with hydrocarbons. *J. Alloy. Compd.* **1992**, *190*, 41–48. [CrossRef]
27. Coey, J.M.D.; Otani, Y. Magnetic properties of $R_2Fe_{17}N_{3-\delta}$. *J. Magn. Soc. Jpn.* **1991**, *15*, 677–684.
28. Li, H.-S.; Coey, J.M.D. Magnetic Properties of Ternary Rare-Earth Transition-Metal Compounds. In *Handbook of Magnetic Materials VI*; Buschow, K.H.J., Ed.; Elsevier: Amsterdam, The Netherlands, 1991.
29. Coey, J.M.D.; Sun, H.; Hurley, D.P.F. Intrinsic magnetic properties of new rare-earth iron intermetallic series. *J. Magn. Magn. Mater.* **1991**, *101*, 310–316. [CrossRef]
30. Harashima, Y.; Terakura, K.; Kino, H.; Ishibashi, S.; Miyake, T. First-Principles Study of Structural and Magnetic Properties of $R(Fe, Ti)_{12}$ and $R(Fe, Ti)_{12}N$ (R = Nd, Sm, Y). *JPS Conf. Proc.* **2015**, *5*, 011021.
31. Kong, L.-S.; Cao, L.; Shen, B.-G. Structures and magnetic properties of the nitrides $(Nd_{1-x}Dy_x)TiFe_{11}N_y$. *J. Magn. Magn. Mater.* **1993**, *124*, 301–304. [CrossRef]
32. Hirayama, Y.; Miyake, T.; Hono, K. Potential and issues of permanent magnet candidate compound $Nd(FeM)_{12}N$ with $ThMn_{12}$-type structure. *Mater. Jpn.* **2016**, *55*, 97–103. [CrossRef]
33. Yang, Y.-C.; Zhang, X.-D.; Kong, L.-S.; Pan, Q. Magnetocrystalline anisotropies of $RTiFe_{11}N_x$ compounds. *Appl. Phys. Lett.* **1991**, *58*, 2042–2044. [CrossRef]
34. Chang, H.; Zhang, X.; Yang, Y. A study on the effect of hydrogen in the compounds with $BaCd_{11}$-type structure. *Solid State Commun.* **2001**, *119*, 403–407. [CrossRef]
35. Miyake, T.; Terakura, K.; Harashima, Y.; Kino, H.; Ishibashi, S. First-Principles Study of Magnetocrystalline Anisotropy and Magnetization in $NdFe_{12}$, $NdFe_{11}Ti$, and $NdFe_{11}TiN$. *J. Phys. Soc. Jpn.* **2014**, *83*, 043702. [CrossRef]
36. Harashima, Y.; Terakura, K.; Kino, H.; Ishibashi, S.; Miyake, T. First-principles study on stability and magnetism of $NdFe_{11}M$ and $NdFe_{11}MN$ for M = Ti, V, Cr, Mn, Fe, Co, Ni, Cu, Zn. *J. Appl. Phys.* **2016**, *120*, 203904. [CrossRef]
37. Fukazawa, T.; Akai, H.; Harashima, Y.; Miyake, T. First-principles study of intersite magnetic couplings in $NdFe_{12}$ and $NdFe_{12}X$ (X = B, C, N, O, F). *J. Appl. Phys.* **2017**, *122*, 053901. [CrossRef]
38. Sato, T.; Ohsuna, T.; Yano, M.; Kato, A.; Kaneko, Y. Permanent magnetic properties of $NdFe_{12}N_x$ sputtered films epitaxially grown on V buffer layer. *J. Appl. Phys.* **2017**, *122*, 053903. [CrossRef]
39. Sepehri-Amina, H.; Tamazawa, Y.; Kambayashi, M.; Saito, G.; Takahashi, Y.K.; Ogawa, D.; Ohkubo, T.; Hirosawa, S.; Doi, M.; Shima, T.; et al. Achievement of high coercivity in $Sm(Fe_{0.8}Co_{0.2})_{12}$ anisotropic magnetic thin film by boron doping. *Acta Mater.* **2020**, *194*, 337–342. [CrossRef]
40. Mao, W.; Zhang, X.; Ji, C.; Chang, H.; Cheng, B.; Yang, Y.; Du, H.; Xue, Y.; Zhang, B.; Wang, L.; et al. Structural and magnetic properties of $PrFe_{12-x}V_x$ and their nitrides. *Acta Mater.* **2001**, *49*, 721–728. [CrossRef]
41. Buschow, K.H.J.; Sherwood, R.C. Magnetic properties and hydrogen absorption in rare-earth intermetallics of the type RMn_2 and R_6Mn_{23}. *J. Appl. Phys.* **1977**, *48*, 4643–4648. [CrossRef]
42. Shiga, M. Magnetism and spin fluctuations of laves phase manganese compounds. *Phys. B + C* **1988**, *149*, 293–305. [CrossRef]
43. Corbett, J.D.; Garcia, E.; Guloy, A.M.; Hurng, W.-M.; Kwon, Y.-U.; Leon-Escamilla, E.A. Widespread Interstitial Chemistry of Mn_5Si_3-Type and Related Phases. Hidden Impurities and Opportunities. *Chem. Mater.* **1998**, *10*, 2824–2836. [CrossRef]
44. Gajdzik, M.; Sürgers, C.; Kelemen, M.; Löhneysen, H.v. Ferromagnetism in carbon-doped Mn_5Si_3 films. *J. Appl. Phys.* **2000**, *87*, 6013–6015. [CrossRef]
45. Sürgers, C.; Gajdzik, M.; Fischer, G.; Löhneysen, H.V.; Welter, E.; Attenkofer, K. Preparation and structural characterization of ferromagnetic $Mn_5Si_3C_x$ films. *Phys. Rev. B* **2003**, *68*, 174423. [CrossRef]
46. Saha, D.K.; Ohshima, K.; Wey, M.Y.; Miida, R.; Kimoto, T. Structure and magnetism of fcc Pd-Mn alloys. *Phys. Rev. B* **1994**, *49*, 15715–15722. [CrossRef] [PubMed]

47. Rashid, M.H.; Sellmyer, D.J. Spin-glass-like freezing in disordered $MnPd_3$ and $CrPd_3$ alloys. *J. Appl. Phys.* **1984**, *55*, 1735–1737. [CrossRef]
48. Sakamoto, Y.; Takao, K.; Nagaoka, Y.; Kida, H.; Flanagan, T.B. Investigations of ordered structures in boron-containing Pd_3Mn alloys. *J. Alloy. Compd.* **1993**, *197*, 35–41. [CrossRef]
49. Kitagawa, J.; Sakaguchi, K. New room-temperature ferromagnet: B-added $Pd_{0.75}Mn_{0.25}$ alloy. *J. Magn. Magn. Mater.* **2018**, *468*, 115–122. [CrossRef]
50. Worsham, J.E., Jr.; Wilkinson, M.K.; Shull, C.G. Neutron-diffraction observations on the palladium-hydrogen and palladium-deuterium systems. *J. Phys. Chem. Solids* **1957**, *3*, 303–310. [CrossRef]
51. Kitagawa, J.; Hara, T.; Sakaguchi, K.; Shirakawa, N.; Tsubota, M. Emergence of room-temperature ferromagnetism in boron-added Mn compounds. In Proceedings of the Joint European Magnetic Symposia 2019, Uppsala, Sweden, 26–30 August 2019; p. 158.
52. Izumi, F.; Momma, K. Three-dimensional visualization in powder diffraction. *Solid State Phenom.* **2007**, *130*, 15–20. [CrossRef]
53. Kotur, B.Y.; Palasyuk, A.M.; Bauer, E.; Michor, H.; Hilscher, G. Uncommon conductivity of R–Mn–Al (R = Gd, Tb) ternary compounds. *J. Phys. Condens. Matter* **2001**, *13*, 9421–9431. [CrossRef]
54. Graf, T.; Felser, C.; Parkin, S.S.P. Simple rules for the understanding of Heusler compounds. *Prog. Solid State Chem.* **2011**, *39*, 1–50. [CrossRef]
55. Sen, S.; Singh, C.; Mukharjee, P.K.; Nath, R.; Nayak, A.K. Observation of the topological Hall effect and signature of room-temperature antiskyrmions in Mn-Ni-Ga D_{2d} Heusler magnets. *Phys. Rev. B* **2019**, *99*, 134404. [CrossRef]
56. Devi, P.; Zavareh, M.G.; Mejía, C.S.; Hofmann, K.; Albert, B.; Felser, C.; Nicklas, M.; Singh, S. Reversible adiabatic temperature change in the shape memory Heusler alloy Ni2.2Mn0.8Ga: An effect of structural compatibility. *Phys. Rev. Mater.* **2018**, *2*, 122401. [CrossRef]
57. Lemoine, P.; Vernière, A.; Mazet, T.; Malaman, B. Magnetic and magnetocaloric properties of R_6Mn_{23} (R = Y, Nd, Sm, Gd-Tm, Lu) compounds. *J. Magn. Magn. Mater.* **2011**, *323*, 2690–2695. [CrossRef]
58. Tsvyashchenko, A.V.; Popova, S.V.; Makhotkin, V.E.; Fradkov, V.A.; Zaritskii, V.N. Investigations of the magnetic properties of the Yb_6Mn_{23} intermetallic compound. *J. Less-Common Met.* **1984**, *96*, 99–102. [CrossRef]
59. Malik, S.K.; Takeshita, T.; Wallace, W.E. Hydrogen induced magnetic ordering in Th_6Mn_{23}. *Solid State Commun.* **1977**, *23*, 599–602. [CrossRef]
60. Bushow, K.H.J. Magnetic properties of the ternary hydrides of Nd_6Mn_{23} and Sm_6Mn_{23}. *Solid State Commun.* **1981**, *40*, 207–210. [CrossRef]
61. Hardman-Rhyne, K.; Rhyne, J.J.; Prince, E.; Crowder, C.; James, W.J. Magnetic and crystallographic structure of $Y_6Mn_{23}D_{23}$. *Phys. Rev. B* **1984**, *29*, 416–422. [CrossRef]
62. Hardman-Rhyne, K.; Kevin Smith, H.; Wallace, W.E. Magnetic and crystallographic structure of $Th_6Mn_{23}D_x$. *J. Less-Common Met.* **1984**, *96*, 201–211. [CrossRef]
63. Pourarian, F.; Boltich, E.B.; Wallace, W.E.; Craig, R.S.; Malik, S.K. Magnetic characteristics of R_6Mn_{23} hydrides (R = Gd, Ho or Er). *J. Magn. Magn. Mater.* **1980**, *21*, 128–132. [CrossRef]
64. Pourarian, F.; Boltich, E.B.; Wallace, W.E.; Malik, S.K. Effect of absorbed hydrogen on magnetic ordering in Tb_6Mn_{23} and Dy_6Mn_{23}. *J. Less-Common Met.* **1980**, *74*, 153–159. [CrossRef]
65. Szytuła, A.; Szott, I. Magnetic properties of ternary RMn_2Si_2 and RMn_2Ge_2 compounds. *Solid State Commun.* **1981**, *40*, 199–202. [CrossRef]
66. Hofmann, M.; Campbell, S.J.; Edge, A.V.J. $EuMn_2Ge_2$ and $EuMn_2Si_2$: Magnetic structures and valence transitions. *Phys. Rev. B* **2004**, *69*, 174432. [CrossRef]
67. Szytuka, A.; Siek, S.; Leciejewicz, J.; Zygmunt, A.; Ban, Z. Neutron diffraction study of UT_2X_2 (T: Mn, Fe, X: Si, Ge) intermetallic systems. *J. Phys. Chem. Solids* **1988**, *49*, 1113–1118. [CrossRef]
68. Fukamichi, K. *Antiferromagnetic Materials*; Kyoritsu: Tokyo, Japan, 2014.
69. Liu, Z.H.; Zhang, Y.J.; Liu, G.D.; Ding, B.; Liu, E.K.; Jafri, H.M.; Hou, Z.P.; Wang, W.H.; Ma, X.Q.; Wu, G.H. Transition from Anomalous Hall Effect to Topological Hall Effect in Hexagonal Non-Collinear Magnet Mn_3Ga. *Sci. Rep.* **2017**, *7*, 515. [CrossRef] [PubMed]
70. Morales, M.; Artigas, M.; Bacmann, M.; Fruchart, D.; Skolozdra, R.; Soubeyroux, J.L.; Wolfers, P. Comparison of the magnetic properties of $ErMn_{12-x}Fe_x$ series with their related hydrides and carbides. *J. Magn. Magn. Mater.* **1999**, *196*, 703–704. [CrossRef]

71. Stankiewicz, J.; Bartolomé, J.; Fruchart, D. Spin Disorder Scattering in Magnetic Metallic Alloys. *Phys. Rev. Lett.* **2002**, *89*, 106602. [CrossRef]
72. Yang, J.B.; Yelon, W.B.; James, W.J.; Cai, S.; Eckert, D.; Handstein, A.; Müller, K.H.; Yang, Y.C. Structural and magnetic properties of $R(Fe_xMn_{1-x})_{12}$ (R = Ho, Y). *Phys. Rev. B* **2002**, *65*, 064444. [CrossRef]
73. Piqué, C.; Blanco, J.A.; Burriel, R.; Abad, E.; Artigas, M.; Fernández-Díaz, M.T. Influence of 3d−4f interactions in the magnetic phases of RFe_xMn_{12-x} (R=Gd, Tb, and Dy) compounds: Coexistence of ferromagnetism and antiferromagnetism at different crystallographic sites. *Phys. Rev. B* **2007**, *75*, 224424. [CrossRef]
74. Kirchmayr, H. Magnetic properties of rare earth–Manganese compounds. *IEEE Trans. Magn.* **1966**, *2*, 493–499. [CrossRef]
75. Muro, Y.; Nakamura, H.; Kohara, T. Magnetism of $ScMn_4Al_8$. In Proceedings of the Physical Society of Japan Autumn Meeting 2005, Kyotanabe, Japan, 19–22 September 2005.
76. Felner, I.; Nowik, I. Magnetism and hyperfine interactions of ^{57}Fe, ^{151}Eu, ^{155}Gd, ^{161}Dy, ^{166}Er and ^{170}Yb in RM_4Al_8 compounds (R = rare earth or Y, M = Cr, Mn, Fe, Cu). *J. Phys. Chem. Solids* **1979**, *40*, 1035–1044. [CrossRef]
77. Bourée-Vigneron, F.; Pinot, M.; Olès, A.; Baran, A.; Suski, W. UCr_4Al_8 and UMn_4Al_8: Neutron diffraction study. *Solid State Commun.* **1990**, *75*, 929–933. [CrossRef]
78. Duong, N.P.; Klaasse, J.C.P.; Brück, E.; de Boer, F.R.; Buschow, K.H.J. Magnetic properties of GdT_4Al_8 and GdT_6Al_6 compounds (T = Cr, Mn, Cu). *J. Alloy. Compd.* **2001**, *315*, 28–35. [CrossRef]
79. Schobinger-Papamantellos, P.; Fischer, P.; de Groot, C.H.; de Boer, F.R.; Buschow, K.H.J. Magnetic properties and neutron diffraction of $TbMn_4Al_8$. *J. Alloy. Compd.* **1996**, *232*, 154–159. [CrossRef]
80. Baran, A.; Suski, W.; Mydlarz, T. Magnetic properties of the (U, Th) $(Cr, Mn)_4Al_8$ compounds. *J. Magn. Magn. Mater.* **1987**, *63*, 196–198. [CrossRef]
81. Fruchart, R.; Roger, A.; Senateur, J.P. Crystallographic and Magnetic Properties of Solid Solutions of the Phosphides M_2P, M = Cr, Mn, Fe, Co, and Ni. *J. Appl. Phys.* **1969**, *40*, 1250–1257. [CrossRef]
82. Srivastava, B.K.; Ericsson, T.; Haggstrom, L.; Verma, H.R.; Andersson, Y.; Rundqvist, S. A Mossbauer study of the $(Fe_{1-x}Mn_x)_2P$ system. *J. Phys. C* **1987**, *20*, 463–472. [CrossRef]
83. Suzuki, N.; Asahi, R.; Kishida, Y.; Masuoka, Y.; Sugiyama, J. Measurement and ab initio calculation of the structural parameters and physical properties of 3d transition intermetallics TiMP (M = Cr, Mn, Fe, Co, or Ni). *Mater. Res. Express* **2017**, *4*, 046505. [CrossRef]
84. Kanomata, T.; Kawashima, T.; Utsugi, H.; Goto, T.; Hasegawa, H.; Kaneko, T. Magnetic properties of the intermetallic compounds MM'X (M = Cr, Mn, M' = Ru, Rh, Pd, and X = P, As). *J. Appl. Phys.* **1991**, *69*, 4639–4641. [CrossRef]
85. Jeitschko, W.; Johnson, V. High pressure Mn_2As with Fe_2P-type structure. *Acta Crystallogr. Sect. B* **1972**, *28*, 1971–1973. [CrossRef]
86. Bartolomé, J.; García, J.; Floría, L.M.; Falo, F.; Navarro, R.; Fruchart, D.; Bacmann, M.; de Jongh, L.J. A magnetic Kosterlitz-Thouless transition in quasi 2-d MnRhAs? *J. Magn. Magn. Mater.* **1986**, *54–57*, 1547–1548. [CrossRef]
87. Bażela, W. Magnetic properties of intermetallic compounds RhMnGe, PdMnGe, $Pd_{1.5}Mn_{0.5}Si$, $Pd_{1.5}Mn_{0.5}Ge$ and RhMnSi. *J. Less-Common Met.* **1984**, *100*, 341–346. [CrossRef]
88. Bazela, W.; Szytuła, A.; Todorović, J.; Tomkowicz, Z.; Zięba, A. Crystal and magnetic structure of NiMnGe. *Phys. Status Solidi A* **1976**, *38*, 721–729. [CrossRef]
89. Brück, E.; van Streepen, T.; Duijn, H.G.M.; Haanappel, E.G.; de Boer, F.R.; Buschow, K.H. J Magnetic and transport properties of $MnPtAl_{1-x}Ga_x$ compounds. *J. Magn. Magn. Mater.* **1988**, *177–181*, 767–768. [CrossRef]
90. Buschow, K.H.J.; De Mooij, D.B. Crystal structure and magnetic properties of PtMnGa and PtMnAl. *J. Less-Common Met.* **1984**, *99*, 125–130. [CrossRef]
91. Kübler, J. Ab initio estimates of the Curie temperature for magnetic compounds. *J. Phys. Condens. Matter* **2006**, *18*, 9795–9808. [CrossRef]
92. Krishnamurthy, V.V.; Kawamura, N.; Suzuki, M.; Ishikawa, T.; Mankey, G.J.; Raj, P.; Sathyamoorthy, A.; Joshi, A.G.; Malik, S.K. Evidence for a magnetic moment on Ir in IrMnAl from x-ray magnetic circular dichroism. *Phys. Rev. B* **2003**, *68*, 214413. [CrossRef]
93. Buschow, K.H.J.; van Engen, P.G.; Jongebreur, R. Magneto-optical properties of metallic ferromagnetic materials. *J. Magn. Magn. Mater.* **1983**, *38*, 1–22. [CrossRef]

94. Masumoto, H.; Watanabe, K. New Compounds of the Clb, Cl Types of RhMnSb, IrMnSn and IrMnAl, New $L2_1$ (Heusler) Type of Ir_2MnAl and Rh_2MnAl Alloys, and Magnetic Properties. *J. Phys. Soc. Jpn.* **1972**, *32*, 281. [CrossRef]
95. Chikazumi, S. *Physics of Ferromagnetism*; Oxford University Press: New York, NY, USA, 1997.
96. Helmholdt, R.B.; Buschow, K.H.J. A neutron diffraction and magnetization study of PdMnTe. *J. Less-Common Met.* **1986**, *123*, 169–173. [CrossRef]
97. Offernes, L.; Ravindran, P.; Kjekshus, A. Prediction of large polar Kerr rotation in the Heusler-related alloys AuMnSb and AuMnSn. *Appl. Phys. Lett.* **2003**, *82*, 2862–2864. [CrossRef]
98. Beckman, O.; Lundgren, L. Compounds of transition elements with nonmetals. In *Handbook of Magnetic Materials*; Buschow, K.H.J., Ed.; Elsevier: New York, NY, USA, 1991; Volume 6, pp. 181–287.
99. Lamichhane, T.N.; Taufour, V.; Masters, M.W.; Parker, D.S.; Kaluarachchi, U.S.; Thimmaiah, S.; Bud'ko, S.L.; Canfield, P.C. Discovery of ferromagnetism with large magnetic anisotropy in ZrMnP and HfMnP. *Appl. Phys. Lett.* **2016**, *109*, 092402. [CrossRef]
100. Ventutini, G.; ljjaali, I.; Ressouche, E.; Malaman, B. Neutron diffraction study of the HoMnSi, LuMnSi and $Sc_{0.9}Lu_{0.1}MnSi$ compounds. *J. Alloy. Compd.* **1997**, *256*, 65–75. [CrossRef]
101. Hoffmann, R.-D.; Pöttgen, R.; Chevalier, B.; Gaudin, E.; Matar, S.F. The ternary germanides UMnGe and U_2Mn_3Ge. *Solid State Sci.* **2013**, *21*, 73–80. [CrossRef]
102. Venturini, G.; Malaman, B.; Ressouche, E. Neutron diffraction study of the TbMnGe compound. *J. Alloy. Compd.* **1996**, *243*, 98–105. [CrossRef]
103. Klosek, V.; Vernière, A.; Ouladdiaf, B.; Malaman, B. Crystal and magnetic structures of the R(=Y, Dy–Tm)MnGe compounds. *J. Magn. Magn. Mater.* **2003**, *256*, 69–92. [CrossRef]
104. Umetsu, R.Y.; Fukamichi, K.; Sakuma, A. Electrical and magnetic properties of antiferromagnetic $L1_0$-type Mn alloys. *Mater. Jpn.* **2004**, *43*, 831–839. [CrossRef]
105. Cui, B.Z.; Marinescu, M.; Liu, J.F. Ferromagnetic Tetragonal $L1_0$-Type MnGa Isotropic Nanocrystalline Microparticles. *IEEE Trans. Magn.* **2013**, *49*, 3322–3325. [CrossRef]
106. Sakuma, A. Electronic Structure and Magnetocrystalline Anisotropy Energy of MnAl. *J. Phys. Soc. Jpn.* **1994**, *63*, 1422–1428. [CrossRef]
107. Suits, J.C. New magnetic compounds with Heusler and Heusler-related structures. *Phys. Rev. B* **1976**, *14*, 4131–4135. [CrossRef]
108. Umetsu, R.Y.; Mitsui, Y.; Yuito, I.; Takeuchi, T.; Kawarada, H. Substitution Effects of Cr or Fe on the Curie Temperature for Mn-Based Layered Compounds MnAlGe and MnGaGe With Cu_2Sb-Type Structure. *IEEE Trans. Magn.* **2014**, *50*, 1–4. [CrossRef]
109. Shibata, K.; Shinohara, T.; Watanabe, H. Magnetic Properties of A New Ferromagnetic Compound MnGaGe. *J. Phys. Soc. Jpn.* **1972**, *32*, 1431. [CrossRef]
110. Matsuzaki, H.; Endo, S.; Notsu, Y.; Ono, F.; Kanomata, T.; Kaneko, T. Pressure Effect on Curie Temperature in MnZnSb. *Jpn. J. Appl. Phys.* **1993**, *32*, 271–272. [CrossRef]
111. Beleanu, A.; Kiss, J.; Kreiner, G.; Köhler, C.; Müchler, L.; Schnelle, W.; Burkhardt, U.; Chadov, S.; Medvediev, S.; Ebke, D.; et al. Large resistivity change and phase transition in the antiferromagnetic semiconductors LiMnAs and LaOMnAs. *Phys. Rev. B* **2013**, *88*, 184429. [CrossRef]
112. Kido, H.; Hoshikawa, T.; Shimada, M.; Koizumi, M. Preparation and magnetic properties of YMnSi. *Phys. Status Solidi A* **1985**, *88*, K39–K43. [CrossRef]
113. Ovtchenkova, I.A.; Nikitin, S.A.; Ivanova, T.I.; Tskhadadze, G.A.; Chistyakov, O.D.; Badurski, D. Magnetocaloric effect and magnetoresistance in $Gd_xLa_{1-x}MnSi$ compounds. *J. Magn. Magn. Mater.* **2006**, *300*, e493–e496. [CrossRef]
114. Welter, R.; Venturini, G.; Ressouche, E.; Malaman, B. Magnetic properties of TbMnSi, determined by susceptibility measurements and neutron diffraction study. *J. Alloy. Compd.* **1994**, *210*, 273–277. [CrossRef]
115. Welter, R.; Venturini, G.; Ressouche, E.; Malaman, B. Neutron diffraction studies of the CeFeSi-type CaMnSi and CaMnGe compounds. *Solid State Commun.* **1996**, *97*, 503–507. [CrossRef]
116. Welter, R.; Venturini, G.; Ressouche, E.; Malaman, B. Crystallographic data and magnetic properties of new CeFeSi-type RMnGe compounds (R = La Sm) studied by magnetization and neutron diffraction measurements. *J. Alloy. Compd.* **1995**, *228*, 59–74. [CrossRef]

117. Dascoulidou, A.; Müller, P.; Bronger, W. Ternäre Mangan-Verbindungen AMnX (A ≙ Mg, Ca, Sr oder Ba; X ≙ Si, Ge oder Sn): Neutronenbeugungsuntersuchungen zur Charakterisierung der magnetischen Eigenschaften. *Z. Anorg. Allg. Chem.* **1998**, *624*, 124–128. [CrossRef]
118. Roger, J.; Yahia, M.B.; Babizhetskyy, V.; Bauer, J.; Cordier, S.; Guérin, R.; Hiebl, K.; Rocquefelte, X.; Saillard, J.-Y.; Halet, J.-F. Mn_5Si_3-type host-interstitial boron rare-earth metal silicide compounds RE_5Si_3: Crystal structures, physical properties and theoretical considerations. *J. Solid State Chem.* **2006**, *179*, 2310–2328. [CrossRef]
119. Mahon, T.; Gaudin, E.; Villesuzanne, A.; Chevalier, B.; Tencé, S. Effect of Carbon Insertion on the Structural and Magnetic Properties of NdScSi. *Inorg. Chem.* **2019**, *58*, 15255–15268. [CrossRef]
120. Coey, J.M.D. New permanent magnets; manganese compounds. *J. Phys. Condens. Matter* **2014**, *26*, 064211. [CrossRef] [PubMed]
121. Tanaka, S.; Terada, H.; Shirakawa, N.; Tsubota, M.; Kitagawa, J. The Impact of the Composition Effect on Ferromagnetic Properties of Tb_2Co_2Ga. *Metals* **2019**, *9*, 1242. [CrossRef]
122. Kitagawa, J.; Takeda, N.; Sakai, F.; Ishikawa, M. Effect of composition in $(RE)_3Pd_{20}Ge_6$ (RE = La, Ce and Nd). *J. Phys. Soc. Jpn.* **1999**, *68*, 3413–3416. [CrossRef]
123. Kitagawa, J.; Terada, H.; Shirakawa, N.; Tsubota, M.; Nose, A.; Tanaka, S. Composition effect in ferromagnetic properties of Tb_3Co_3Ga. *Results Phys.* **2019**, *15*, 102591. [CrossRef]
124. Lu, Q.M.; Yue, M.; Zhang, H.G.; Wang, M.L.; Yu, F.; Huang, Q.Z.; Ryan, D.H.; Altounian, Z. Intrinsic magnetic properties of single-phase $Mn_{1+x}Ga$ ($0 < x < 1$) alloys. *Sci. Rep.* **2015**, *5*, 17086.
125. Enkovaara, J.; Heczko, O.; Ayuela, A.; Nieminen, R.M. Coexistence of ferromagnetic and antiferromagnetic order in Mn-doped Ni_2MnGa. *Phys. Rev. B* **2003**, *67*, 212405. [CrossRef]
126. Larson, P.; Mazin, I.I.; Papaconstantopoulos, D.A. Effects of doping on the magnetic anisotropy energy in $SmCo_{5-x}Fe_x$ and $YCo_{5-x}Fe_x$. *Phys. Rev. B* **2004**, *69*, 134408. [CrossRef]
127. Sakuma, A.; Manabe, Y.; Kota, Y. First principles calculation of magnetocrystalline anisotropy energy of MnBi and $MnBi_{1-x}Sn_x$. *J. Phys. Soc. Jpn.* **2013**, *82*, 073704. [CrossRef]
128. Pandey, T.; Parker, D.S. Magnetic properties and magnetocrystalline anisotropy of Nd_2Fe_{17}, $Nd_2Fe_{17}X_3$, and related compounds. *Sci. Rep.* **2018**, *8*, 3601. [CrossRef]
129. Miyahara, J.; Shirakawa, N.; Setoguchi, Y.; Tsubota, M.; Kuroiwa, K.; Kitagawa, J. Hill plot focusing on Ce compounds with high magnetic ordering temperatures and consequent study of Ce_2AuP_3. *J. Supercond. Nov. Magn.* **2018**, *31*, 3559–3564. [CrossRef]
130. Yamada, Y.; Ueno, K.; Fukumura, T.; Yuan, H.T.; Shimotani, H.; Iwasa, Y.; Gu, L.; Tsukimoto, S.; Ikuhara, Y.; Kawasaki, M. Electrically Induced Ferromagnetism at Room Temperature in Cobalt-Doped Titanium Dioxide. *Science* **2011**, *332*, 1065–1067. [CrossRef] [PubMed]
131. Kitagawa, J.; Kitajima, D.; Shimokawa, K.; Takaki, H. Photoinduced Kondo effect in $CeZn_3P_3$. *Phys. Rev. B* **2016**, *93*, 035122. [CrossRef]
132. Stewart, G.R. Non-Fermi-liquid behavior in *d*- and *f*-electron metals. *Rev. Mod. Phys.* **2001**, *73*, 797–855. [CrossRef]
133. Eom, D.; Ishikawa, M.; Kitagawa, J.; Takeda, N. Suppression of Antiferromagnetism by Kondo Effect and Quantum Critical Behavior in $CeCoGe_{3-x}Si_x$ ($0 \leq x \leq 3$). *J. Phys. Soc. Jpn.* **1998**, *67*, 2495–2500. [CrossRef]
134. Custers, J.; Gegenwart, P.; Wilhelm, H.; Neumaier, K.; Tokiwa, Y.; Trovarelli, O.; Geibel, C.; Steglich, F.; Pépin, C.; Coleman, P. The break-up of heavy electrons at a quantum critical point. *Nature* **2003**, *424*, 524–527. [CrossRef]
135. Löhneysen, H.V.; Rosch, A.; Vojta, M.; Wölfle, P. Fermi-liquid instabilities at magnetic quantum phase transitions. *Rev. Mod. Phys.* **2007**, *79*, 1015–1075. [CrossRef]
136. Huang, C.-L.; Hallas, A.M.; Grube, K.; Kuntz, S.; Spieß, B.; Bayliff, K.; Besara, T.; Siegrist, T.; Cai, Y.; Beare, J.; et al. Quantum Critical Point in the Itinerant Ferromagnet $Ni_{1-x}Rh_x$. *Phys. Rev. Lett.* **2020**, *124*, 117203. [CrossRef]
137. Akayama, M.; Fujii, H.; Yamamoto, K.; Tatami, K. Physical properties of nitrogenated $RFe_{11}Ti$ intermetallic compounds (R = Ce, Pr and Nd) with $ThMn_{12}$-type structure. *J. Magn. Magn. Mater.* **1994**, *130*, 99–107. [CrossRef]